Building and Environment 266 (2024) 112077

Contents lists available at ScienceDirect

Building and Environment

journal homepage: www.elsevier.com/locate/buildenv

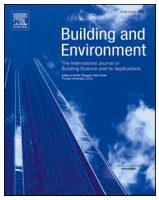

Natural ventilation in large spaces: CFD simplified model validated with full-scale experimental data of Roman Baths

Rafaela Mateus [a,b,*], Armando Pinto [b], José M.C. Pereira [a]

[a] LAETA, IDMEC, Instituto Superior Técnico, Universidade de Lisboa, Mechanical Engineering Department/LASEF, Av.Rovisco Pais, 1, Lisbon, 1049-001, Portugal
[b] NAICI, Laboratório Nacional de Engenharia Civil, Buildings department, Av. do Brasil 101, 1700-075, Lisboa, Portugal

ARTICLE INFO

Keywords:
Natural ventilation
Large spaces
CFD model
In-situ
Air distribution
Performance

ABSTRACT

This study addresses the escalating need for energy-efficient and well-ventilated buildings by examining natural ventilation in large spaces. Validation of a CFD model was pursued through *in-site* experiments at the Roman Baths Museum in Chaves, Portugal. A sensitivity analysis aimed to determine the optimal number of monitoring points for model validation, crucial for establishing procedures in large-volume settings. Findings emphasized the feasibility of using a minimal number of monitored points, notably with a 3 × 3 test point arrangement, showcasing consistent temperature variations with low relative errors (0.50 %–1.75 %). Furthermore, the validated model assessed ventilation performance under diverse operational conditions, revealing slight enhancements in experimental settings, including an increase in air change rate (2.4 vs. 2.2 ACH) and a decrease in buoyancy dominance (Richardson number 197.3 vs. 241.3) compared to design conditions. Quantitative analysis highlighted similar temperature and velocity trends, with greater stratification in experimental conditions (temperature ratios 0.12 to 0.36 vs. 0.10 to 0.32). Qualitative assessments align with the quantitative analysis and enable the identification of stagnation zones and airflow distribution patterns. These findings affirm the methods' reliability in analysing ventilation in large spaces naturally ventilated, validating the model across diverse contexts, despite fewer data points.

1. Introduction

In recent decades, there has been a notable increase in the utilization of mechanical cooling systems in buildings, driven by factors such as global warming, higher internal heat gains, widespread adoption of unshaded glazed facades, and stricter thermal comfort requirements [1]. In response to this trend, designers are encouraged to adopt natural ventilation (NV) strategies as a means to mitigate energy consumption and enhance indoor air quality [2–4].

While NV systems offer sustainable benefits with lower investment costs and no fan energy consumption compared to mechanical ventilation systems [5–7], their applicability is limited in buildings with large air volumes such as sports complexes and indoor pools. Mechanical or hybrid ventilation solutions often become the preferred choice for such structures, albeit at the expense of increased energy consumption [8–12].

Extensive literature reviews have been conducted on NV, examining its evolution, ideal configurations, experimental techniques, numerical simulation methods, and application to sustainable buildings [4,11–22]. Understanding natural convection and its role in energy performance and indoor air quality (IAQ) is crucial for achieving energy efficiency targets, particularly in Nearly Zero Energy Buildings (NZEB) [23].

Efforts to enhance energy efficiency in buildings are paramount for mitigating greenhouse gas emissions and combating climate change. With the building sector accounting for a significant portion of global emissions, initiatives like the Paris Agreement and the Europe Union's targets emphasize the importance of reducing carbon footprints [24,25]. Addressing energy poverty is also critical, as inadequate heating can lead to health issues and social exclusion [26–28]. The literature review [29] conducted by the authors revealed several key insights regarding the study of NV in different spatial contexts.

Firstly, it was noted that full-scale models of normal spaces are more commonly studied compared to large spaces. These studies typically measure parameters such as temperature, velocity, and relative humidity at various points, with measurement durations typically spanning weeks. However, there is variability in the number and location of

* Corresponding author. LAETA, IDMEC, Instituto Superior Técnico, Universidade de Lisboa, Mechanical Engineering Department/LASEF, Av.Rovisco Pais, 1, Lisbon, 1049-001, Portugal.
E-mail address: rafaela.mateus@tecnico.ulisboa.pt (R. Mateus).

https://doi.org/10.1016/j.buildenv.2024.112077
Received 26 June 2024; Received in revised form 18 August 2024; Accepted 9 September 2024
Available online 10 September 2024

measurement points, which impacts the accuracy of the results. Additionally, there is a lack of studies that encompass both winter and summer seasons.

In contrast, full-scale models of large spaces are less frequently examined, but when studied, velocity and temperature are the primary parameters measured at selected points. Gaps were identified in terms of the number and location of measurement points, highlighting the need for optimization in monitoring spaces with high dimensions.

Regarding computational fluid dynamics (CFD) modelling, it was found that turbulence models such as standard k– ε, RNG k– ε, realizable k-ε and k-ω SST are commonly applied. For studies of large spaces, there is a preference for category k– ε models due to their lower computational requirements. Experimental data, particularly from small-scale models in wind tunnels, are commonly used for model validation, with velocity being a key validation parameter. While full-scale models are less utilized for model calibration, they are still valuable for studies conducted in controlled environmental conditions.

Overall, there is a clear need to further develop studies focusing on large spaces, incorporating sensitivity analyses of monitoring point locations and numbers. Establishing standardized procedures for *in-situ* experimentation in buildings with large air masses is crucial for ensuring the reliability of CFD models.

To address these aspects, this study aims to validate a CFD model suited for analysing large spaces with numerous radiators, using *in-situ* experimental measurements conducted at the Roman Baths Museum in Chaves, Portugal. The study includes a sensitivity analysis to determine the number of monitoring points required to validate the model, aiming to establish benchmarks that serve as inputs to assist in decision-making for validating models of large volumes, specifically considering the limitation in the number of available monitoring equipment and the extensive volume of the spaces. Additionally, the study explores the application of the validated model to assess the ventilation performance under various scenarios with differing operational conditions. Evaluating ventilation performance in large spaces naturally ventilated presents challenges due to complex air distribution patterns; therefore, the goal is to verify if performance can be consistently assessed both qualitatively and quantitatively through four distinct methods.

2. Methodology

To explore natural ventilation in large spaces, it was necessary to conduct an experimental campaign covering the entire area, allowing the establishment of indicators for the experimental procedure needed to validate the respective numerical models, which will be used to evaluate/optimize natural ventilation in such spaces. Fig. 1 specifies the two components of the methodology used in this study: the experimental component and the numerical component. The experimental component was divided into two measurement stages, designated as follows:

1. Control, where indoor ambient conditions were monitored, occurring simultaneously with stage 2.
2. Indoor air, where air temperature and velocity are monitored at a network of points covering the entire area of the two floors of the thermal baths (basement and ground floor).

Meanwhile, the simulation component consisted of two stages:

3. CFD validation, where model simplifications are applied and validated with experimental data obtained in the experimental component.
4. CFD scenarios, where the validated model is applied to two scenarios with experimental and design operating conditions, aiming to investigate their influence on the performance of natural ventilation.

3. Description of the Roman Baths

The experimental setup involved the Roman Baths Museum building in Chaves, Portugal, depicted in Fig. 2(a). This building encompasses a spacious area accommodating the Roman Baths and adjacent zones spread across two levels: one below ground level, referred to as the basement floor (BF), housing the pools, Fig. 2(b), and one above ground level, referred to as the ground floor (GF), where museum visitors circulate, Fig. 2(c).

The building's main facade is oriented towards the southwest. Inside the Roman Baths area, the ceiling stands at approximately 8 m high, enclosing a total volume of about 11,600 m^3. The Roman Baths space encompasses four pools under study (Fig. 2(d)), each with distinct water temperatures [10]: Pool B at 36 °C, Pool A with ambient temperatures ranging from 10 to 20 °C, Water conduit at 44 °C, and Reservoir at 48 °C. Situated at an elevation of 350 m, the building's raised section, measuring less than 6 m in height, is sheltered from wind by nearby structures, categorizing it under wind exposure region A with aerodynamic roughness category I [10,30–32]. It falls within climatic zone I2, V3 as per Portugal's Building Energy Certification System [33]. Ventilation in the thermal bath area relies on pressure differentials caused by temperature differences and wind effects through openings in the roof and walls. The building features seven air intake openings in the facade wall and two above the emergency exit door, all controlled by automatic mechanisms. The project's opening areas correspond to 5.6 m^2 for the openings in the facade wall and 3.60 m^2 above the emergency exit door [30]. Additionally, there are twenty-eight ventilation grilles on roof, each with a free area of 0.27 m^2, totaling approximately 7.6 m^2 of free opening area. Heating is provided by a system of hot water radiators, with a heat exchanger facilitating heat transfer between primary and secondary circuits. The radiators, totaling 130 in number and comprising 1038 elements, are made of die-cast and extruded aluminium with a black finish for architectural appeal. Furthermore, the building is equipped with a ventilation monitoring system,

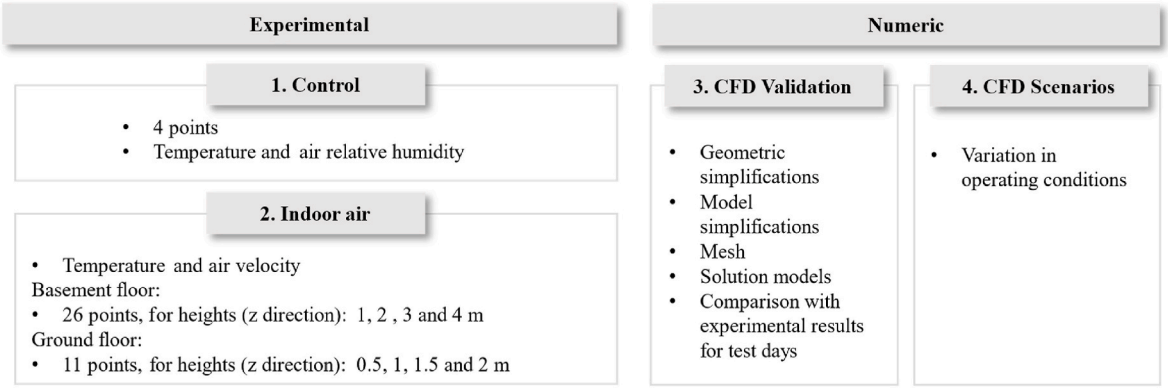

Fig. 1. The two components of the methodology and their respective stages.

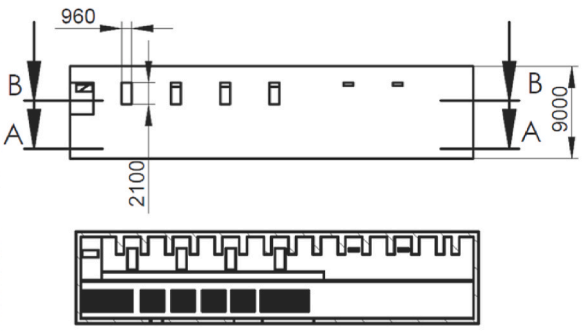

(a) Overview of Roman Baths and identification of cuts plans

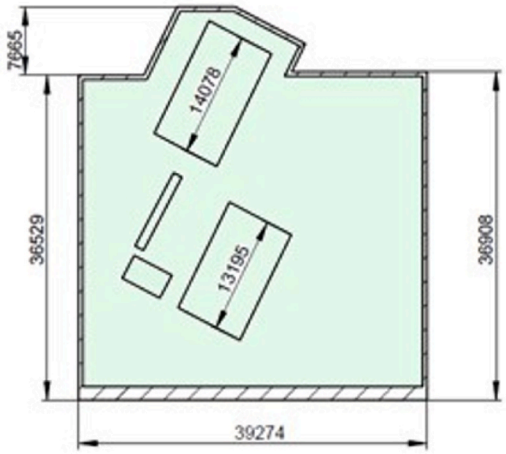

(b) Basement floor plan (Section A -A)

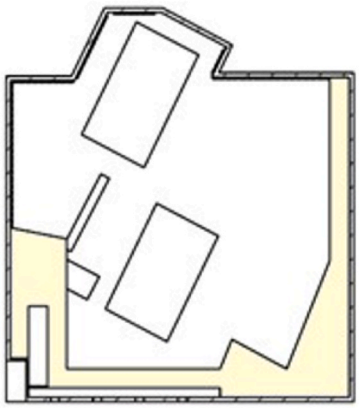

(c) Ground floor plan (Section B -B)

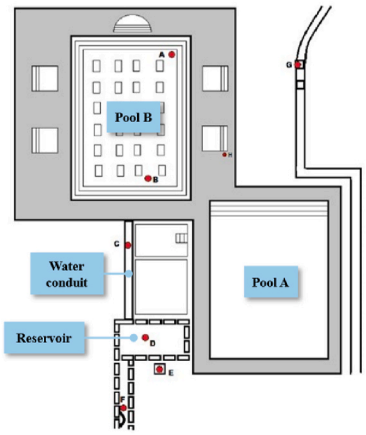

(d) Identification of water plans

Fig. 2. Roman baths museum in Chaves.

incorporating probes for temperature, humidity, and wind speed both inside and outside the building, ensuring effective operation.

According to the project specifications [30], the system operates with an inlet temperature of 55 °C and an outlet temperature of 25 °C, resulting in a temperature jump of 30 °C. The average temperature is maintained at 40 °C, while room temperature is set at 18 °C, resulting in a temperature difference of 22 °C. Each radiator element generates a heat output (Q) of 106 W, with a total heat output (Q50 - Heat output corresponding to $\Delta T = 50$ °C (Normal Conditions)) of 321 W per element. The system's thermal requirements are estimated at 110 kW.

4. Experimental component

4.1. Measurement setup

The measurement setup monitored the interior conditions of the Roman Baths. The experimental tests were conducted on January 16th and 17th, 2024, between 7 a.m. and 12 p.m. Regarding the number and location of measurement points, their selection was based on extensive research work [29]. Despite the conclusions indicating that there is no defined procedure, there are some common lines, such as using a column to assess at various heights and considering multiple points to cover the spaces [1,34–36].

In this study, the experimental component encompasses three stages, as depicted in Fig. 1. The control stage involves the installation of four probes according to Fig. 3(a) to monitor the temperature and relative humidity of the space. Specifically, three of the points (C2 to C4) coincide with the positions of three probes from the ventilation monitoring system, as they were placed in non-visible places, close to cable support and accessible locations. These three points are situated roughly at ground floor level ($z \approx 3.5$ m), whereas point C1 is positioned near the centre of the basement floor, approximately 1.5 m above ground level. Data acquisition occurred at a rate of every 5 min throughout the entirety of the test days, and this phase occurs independently from the others.

In the indoor air stage meticulous monitoring was conducted across two critical areas: the ground floor and the basement floor. For the ground floor analysis, a network of 11 monitoring points was strategically deployed to capture comprehensive data. Among these, seven points were strategically positioned within the vicinity of facade openings to capture airflow in the y-direction, at 1.5 m from the opening. The remaining three points were designated to assess the impact of thermal plumes generated by radiators, particularly in areas of the deck further from the openings where the predominant airflow direction was z-direction. Fig. 3(b) provides clarity on the exact positioning of these monitoring points. Points 1 to 7 were situated 0.5 m from the display counter, while the remaining points were placed 2 m from the wall. The probes were positioned 0.5 m from the support rod to avoid interference. However, for points 8 to 11, the distance was extended to 0.9 m above the railing to monitor the thermal plume effect. The precise placement of the monitoring probes is visually outlined in Fig. 3(b), with a consistent vertical spacing of 0.5 m between probes to ensure comprehensive

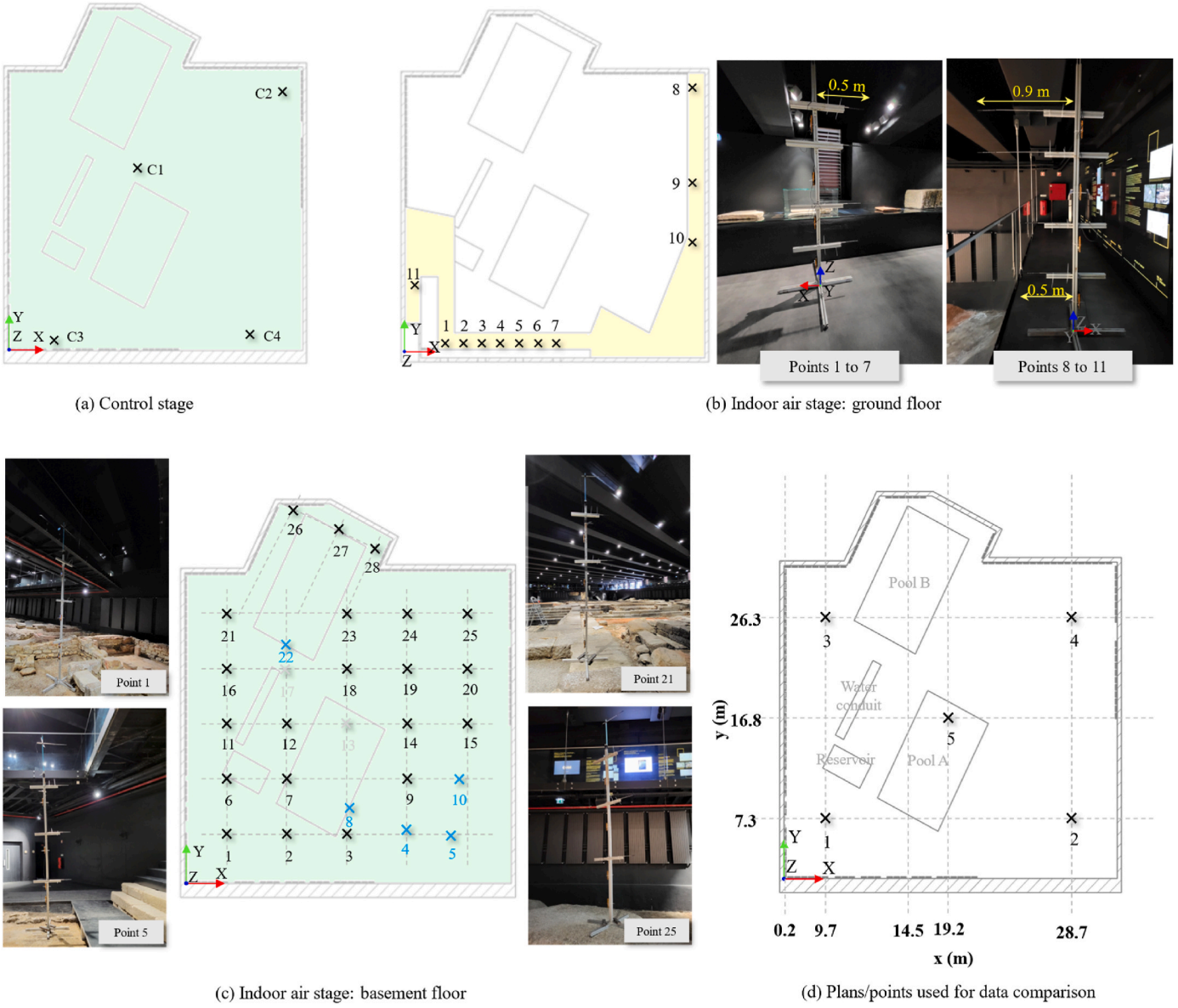

(a) Control stage

(b) Indoor air stage: ground floor

(c) Indoor air stage: basement floor

(d) Plans/points used for data comparison

Fig. 3. Measurement points and planes/points used for experimental and CFD comparison.

coverage and accurate data collection.

For the basement floor assessment, an extensive approach was taken by establishing a matrix consisting of a 5 b y 5 grid of monitoring points (nearly 27 m × 27 m), as depicted by the dashed lines in Fig. 3(c). Additionally, three supplementary points were strategically located in the region behind pool B, resulting in a total of 28 monitoring points. This meticulous selection aimed to provide extensive coverage across the entire area of interest, facilitating a detailed analysis of the model's validation process concerning varying point densities. However, it's worth noting that due to the specific layout and features of the baths, two points within the initial matrix proved entirely inaccessible (points 13 and 17), while five other points necessitated slight displacement either along the x or y direction to accommodate site constraints. These adjustments were highlighted in blue in Fig. 3(c), and correspond to points 4, 5, 8, 10 and 22. After applying these conditioning factors, the total number of accessible points is 26. For a visual reference of the exact locations of all monitoring points and the detailed arrangement of the monitoring probes, please consult Fig. 3(c). The figure illustrates the positions of the monitoring points and the spacing of 1 m between probes. Each probe is 0.5 m in length, ensuring optimal performance and reliability throughout the duration of the experiment.

A temperature data logger was employed to continuously monitor the room temperature and relative humidity under ambient conditions. Thermo-anemometers, outfitted with hot wire probes, were utilized to measure both the air velocity and temperature above the radiators. Furthermore, a thermal camera with an emissivity of 0.9 was employed to assess the temperature of the radiators. The specifications of each measurement device are detailed in Table 1.

4.2. Measurement results

The analysis commences by scrutinizing the outdoor conditions, focusing on the evolution of outdoor temperature and relative humidity. For both days, the average outdoor temperature hovers around 12 °C, exhibiting a marginal difference of merely 0.3 °C between them. Likewise, the average relative humidity remains constant at 67.6 % throughout the observed period. However, delving deeper into the data reveals that temperature fluctuations are more pronounced on January 16, 2024, compared to January 17, 2024.

During the control stage, the indoor temperature and relative

Table 1
Specifications of measuring equipment.

Equipment		Range		Uncertainty	Resolution
		Min	Max		
Humidity and temperature data logger	Humidity (%)	0	100	±1.5	0.01
	Temperature (°C)	−30	70	±0.2	0.01
Thermo-anemometers (Hot wire probe)	Velocity (m/s)	0.3	35	±(0.1 m/s + 1.5 % of mv[a]) (0.3–20 m/s) ±(0.2 m/s + 1.5 % of mv[a]) (20–35 m/s)	0.01
	Temperature (°C)	−20	70	±0.5	0.1
Thermal Camera	Temperature (°C)	0	350	–	0.1

[a] mv corresponds to the measured value.

humidity conditions of the Baths were monitored at four points (see Fig. 3(a)). Point C1 was situated approximately at the centre of the basement floor at a height (z) of around 1.5 m, and points C2 to C4 were located where three of the ventilation monitoring system's probes were, approximately at ground floor level (z ≈ 3.5 m). The average values for the internal temperature and relative humidity for the four measurement points were graphically represented in Fig. 4 and indicated that for both days, the average temperature of the four points was approximately 25.1 and 24.4 °C for January 16 and 17, 2024, respectively, and the average relative humidity corresponded to 55.6 and 55.4 %. Although the average temperature difference was only 0.7 °C between two days, it was noteworthy that the maximum average temperature was recorded at probe C2, which was approximately 8 °C higher than probe C1 (located at the centre of the room), and that for probe C3, there was also a difference from probe C1, but smaller, on the order of 5 °C. Probes C1 and C4 recorded very close average values. Regarding relative humidity, it followed the temperature trends but with less pronounced variation. Given that permanent probes located at the points of the C1 to C4 probes control the ventilation system, it was expected that they would be located at points where the temperature was similar among them, or in points that were not directly influenced by heat sources. However, the sensor location is restricted by the visual impact and cable pathways available and the data showed that there were at least two points that were being influenced by the air flow from heat sources and increased the average value of indoor temperature compared to the temperature at basement floor (z = 1.5 m).

In the indoor air stage monitoring, air temperature and velocity were monitored in two critical areas: the ground floor and the basement floor. For the ground floor analysis, a network of 11 monitoring points was strategically deployed to capture comprehensive data, as depicted in Fig. 3(b). For the assessment of the basement floor, 26 points were monitored, in accordance with the layout shown in Fig. 3(c). Additionally, surface temperatures of the radiators installed in the Roman Baths were recorded.

On the ground floor, temperature and air velocity were measured at four heights (0.5, 1, 1.5, and 2 m) to assess thermal and airflow conditions. Analysis of the data represented in Fig. 5(a) showed temperature differences between heights near building openings, ranging from 2 to 4 °C on January 16 and 17. At 1.5 and 2 m, temperatures remained consistent with small variations of about 0.3 °C. Points farther from the facade exhibited uniform temperatures around 24 °C. Air velocities near openings ranged from 0 to 0.4 m/s, decreasing significantly at 2 m height, indicating descending airflow. In areas away from openings, the highest velocities occurred at 1.5 m height, suggesting thermal plumes bypassing the ground floor deck. Overall, the study reveals the intricate relationship between thermal conditions and airflow dynamics on the ground floor, with consistent trends.

On the basement floor, temperature and air velocity were measured at four heights (1, 2, 3, and 4 m) at 26 points. Results presented in Fig. 5 (b) showed a consistent vertical temperature gradient with slightly higher average values on January 16 compared to January 17, about 0.7 °C difference. The highest temperatures were observed at points 27 and 28, located 4 m high, near the bottom area of the baths. Velocity measurements fell below 0.06 m/s across all elevations, making them inadequate for CFD model validation, as these values are lower than the measurement equipment's uncertainty. Finally, the distribution of average temperature over the two days of testing is depicted relative to the locations of the monitored points in the baths (Fig. 6(a)).

CFD model validation was carried out using temperature data for the four planes; however, a sensitivity analysis was performed on the number of monitored points required to validate the model, aiming to establish benchmarks for a generic procedure for validating models with large volumes. Three scenarios were considered for this analysis: the first scenario involves the total number of points, averaging the parameters for all 26 points; the second scenario includes 11 points (based on a 3 × 3 grid and the two extreme points in the deepest area of the baths); and the third scenario considers only 6 points (based on a cross pattern, including points 1, 5, 18, 21, 25, and 27). Only the points from the basement floor were used because they are not directly affected by heat sources and air openings, ensuring a more representative validation of the internal conditions.

From the analysis of the average temperatures for each plane over the two days of testing, as shown in Table 2 and Fig. 6(b), relative errors are observed in the scenarios of 11 and 6 points compared to the more accurate scenario with 26 points, ranging between 0.5 % and 0.8 % for the 11-point scenario and between 1 % and 1.75 % for the 6-point scenario. With such low relative errors (less than 5 %), we can draw some conclusions. It was found that in this type spaces with large naturally ventilated air masses, temperature variations at a certain height plane are practically constant. Therefore, using a reduced number of points does not significantly affect the average temperatures on that plane. This suggests that the validation process may be independent of the number of points, allowing us to optimize the number of experimentally monitored points required to validate the model in such environments.

In this regard, it is proposed that the testing procedure for large

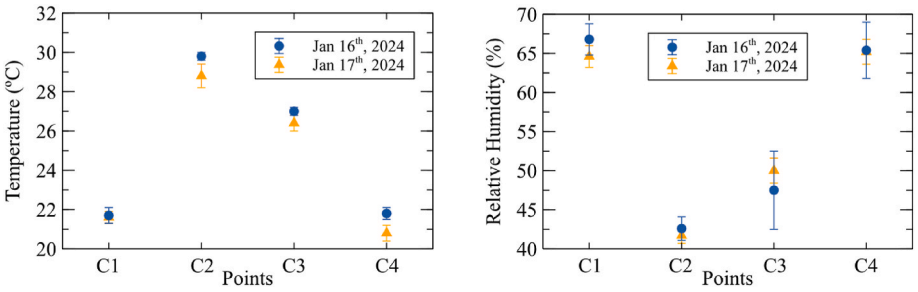

Fig. 4. Indoor temperature and relative humidity average for the control stage (to locate C1 to C4, refer to Fig. 3(a)).

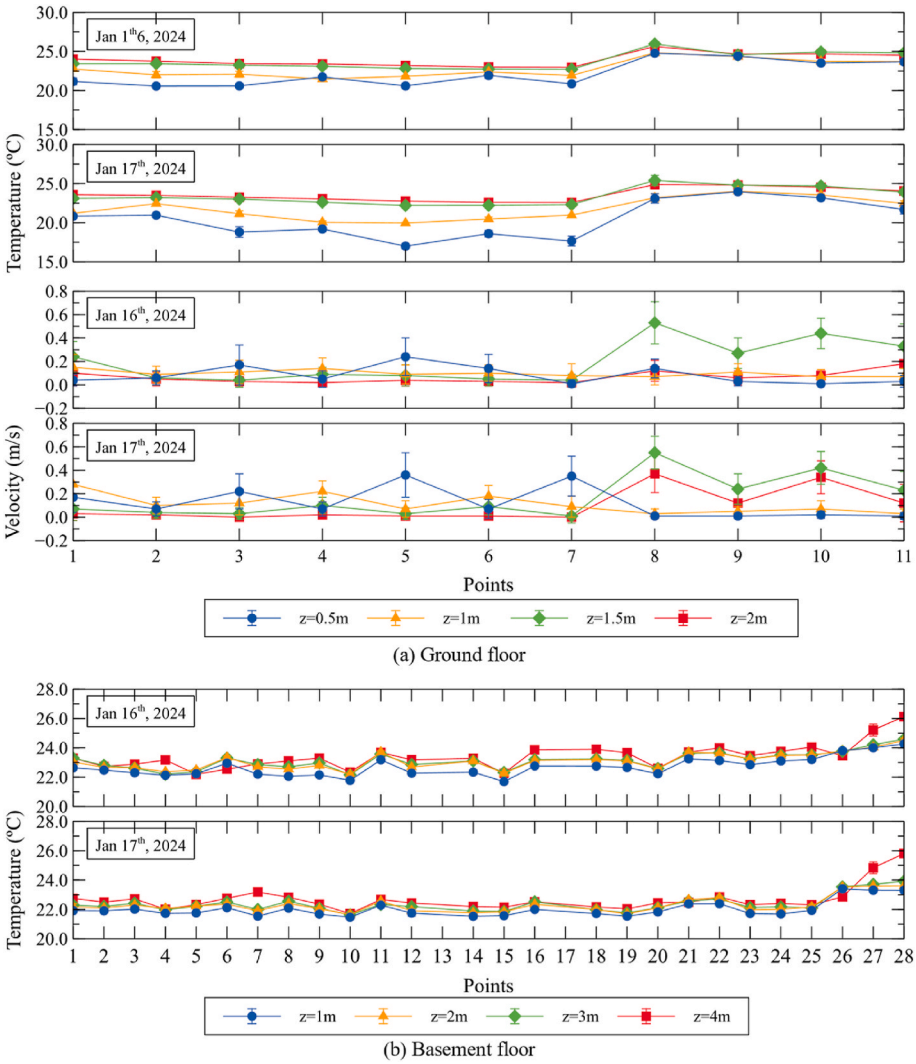

Fig. 5. Temperature and velocity at monitoring points for the indoor air stage.

naturally ventilated spaces defines test points in a 3 × 3 matrix, selecting the main area of the space and collecting points at the four corners of each side, as well as the central point. Additionally, one or more points should be included in different zones that do not fit the square geometry of the space. Moreover, the main matrix should be about 5 m away from the heat sources of the walls, ensuring that we are validating the model within the current zone of interest.

5. CFD simulation

5.1. CFD methodology

The numerical component described in Fig. 1 encompasses two stages, both of which involve conducting Computational Fluid Dynamics (CFD) simulations utilizing the STAR-CCM + software. This software employs the finite volume method (FVM) to solve the fundamental equations governing fluid mechanics and heat transfer. The CFD methodology, outlined in Fig. 7, was applied in two steps to create a validated operational model that demands low computational resources. This model was utilized to evaluate heat transfer from water to the radiator and from the radiator surface to the environment, specifically considering natural convection buoyancy (plume) induced by the heated radiator surfaces. The methodology relies on a simplified model well-suited for analysing large air volumes while accurately predicting thermal plumes. Its efficacy has been demonstrated in prior research [37].

In Step 1, two parallel models were constructed. Firstly, a 1/2-Element Model of the radiator was developed, encompassing all three regions (liquid, solid, and gas). To ascertain the convection coefficient (h) within the desired operational range, a minimum of six simulations are conducted. This coefficient is then interpolated for all conditions within the specified range. Additionally, viscous, and inertial resistance coefficients (K_v and K_i) were derived, representing characteristics of the porous media. Secondly, a 1-Element Model of the radiator was created, focusing solely on the solid region. The model underwent a temperature variation process to determine the material's equivalent conductivity in each direction. Subsequently, this conductivity data was integrated into the simplified model.

In Step 2, a Simplified Model was developed employing a porous media (PM) approach to represent the 130 radiators. This model incorporates the properties determined in Step 1. The results obtained from this Simplified Model were then compared with the experimental results. If the discrepancy between these results is less than 10 %, the process is considered complete, and the model is deemed operational for conducting sensitivity studies and developing more effective strategies for managing natural ventilation in spaces with large masses of air and without controlled environmental conditions.

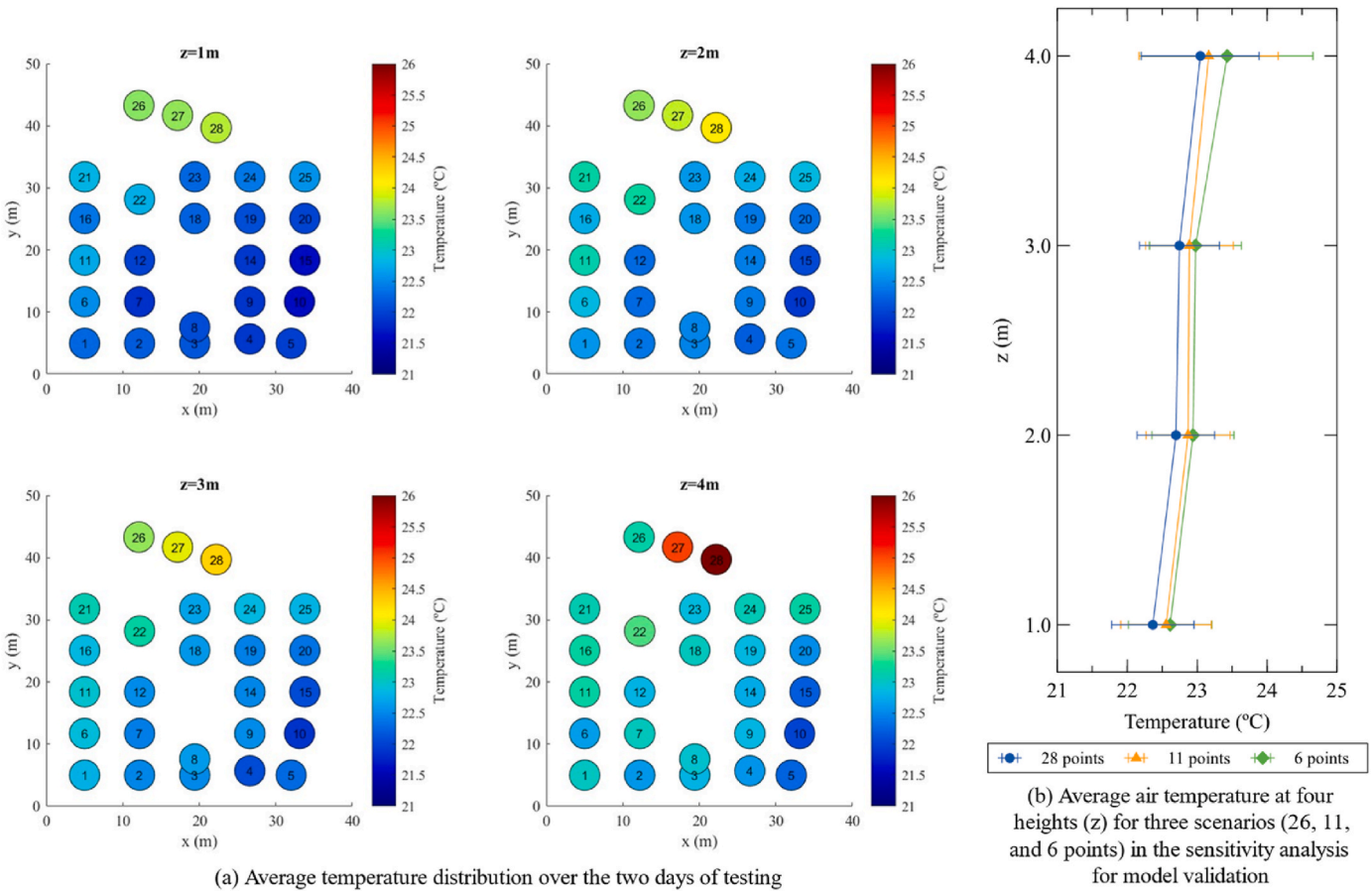

(a) Average temperature distribution over the two days of testing

(b) Average air temperature at four heights (z) for three scenarios (26, 11, and 6 points) in the sensitivity analysis for model validation

Fig. 6. Overview of temperature distribution on the basement floor and model validation sensitivity analysis.

Table 2
Average temperature on the basement floor at four heights (z) in [°C] for the indoor air stage.

	Planes			
	z = 1 m	z = 2 m	z = 3 m	z = 4 m
28 points	22.4	22.7	22.7	23.0
11 points	22.6	22.9	22.9	23.2
6 points	22.6	22.9	23.0	23.4
RE (11 points) [%][a]	0.85	0.76	0.62	0.52
RE (6 points) [%][a]	1.11	1.07	1.02	1.66

[a] RE is the relative error considering the data from the 28 points as the most accurate value.

5.2. Models and governing equations

The investigation addressed the problem by employing governing equations for three-dimensional, turbulent flow and incompressible fluid. Heat transfer within the radiator's water channels occurred through forced convection as hot water circulated, subsequently conducting heat through the radiator panels and warming the surrounding air. The Boussinesq approximation was utilized to model natural convection airflow, while radiation heat loss was accounted for using the surface-to-surface (S2S) model. Unsteady-state models were employed in the study, utilizing a time step of 0.01 s.

The equations of mass conservation, linear momentum conservation, and energy conservation in enthalpy form [38] were solved using the SIMPLE algorithm (Semi-Implicit Method for Pressure Linked Equations). The mass and momentum equations were independently solved, and pressure was corrected based on a predictive-corrective model. Upon discretizing the domain, the software solved these equations by integrating over the control volume. Turbulence effects were accounted for through the RANS model, employing the Realizable k-ε Two-Layer turbulence model. This model solved two equations—one for turbulent kinetic energy and another for turbulence dissipation rate. Within this framework, the flow was treated as fully turbulent, rendering the effects of molecular viscosity negligible due to turbulent diffusion.

The radiator's complex geometry was simplified using a porous media (PM). PM, was defined as a solid allowing fluid passage, facilitated governing flow and heat transfer by replacing the radiator and modifying equations. This model was based on Darcy-Forchheimer's law, distinguishing between two resistances: viscous (from friction-induced stresses) and inertial (from flow profile) [39]. Solid porosity, characterized by Equation (1), was crucial for solving flow and heat transfer equations in PM (Equations (2) and (3)) [38]. The software used offers two porous media energy models: equilibrium and non-equilibrium. The equilibrium model assumes fluid and solid temperatures in porous media are equal, suitable for fast thermal response times and instantaneous heat exchange. Conversely, the non-equilibrium model considers independent fluid and solid temperatures, simulating situations with slower thermal response times and significant thermal imbalances. In this study, the non-equilibrium model was chosen for better representing reality, distinguishing between phases while maintaining respective properties.

$$\chi = \frac{V_f}{V} \tag{1}$$

$$\frac{\partial \chi \rho}{\partial t} + \nabla \cdot (\rho \chi \mathbf{v}) = 0 \tag{2}$$

$$\frac{\partial \chi \rho \mathbf{v}}{\partial t} + \nabla \cdot (\rho \chi \mathbf{v}\mathbf{v}) = -\chi \nabla \mathrm{p} + \nabla \cdot (\chi \mathbf{T}) - \chi \mathbf{P_v} \mathbf{v_s} - \chi \mathbf{P_i} |\mathbf{v_s}| \mathbf{v_s} \tag{3}$$

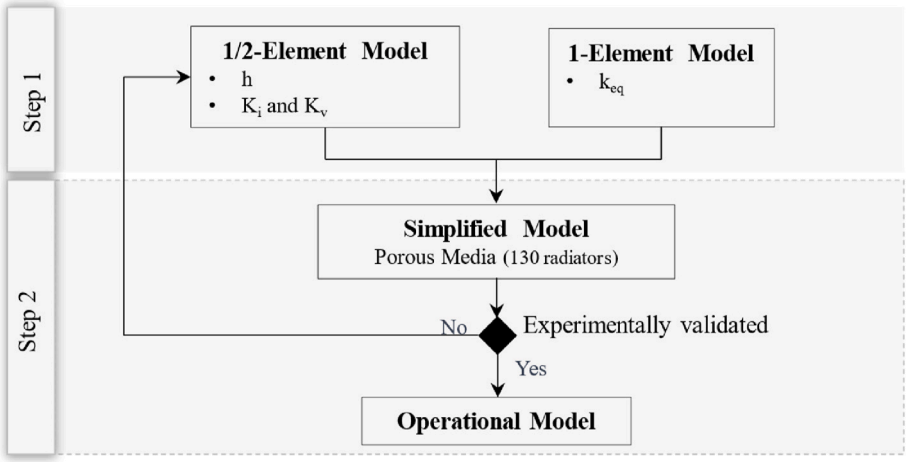

Fig. 7. CFD methodology.

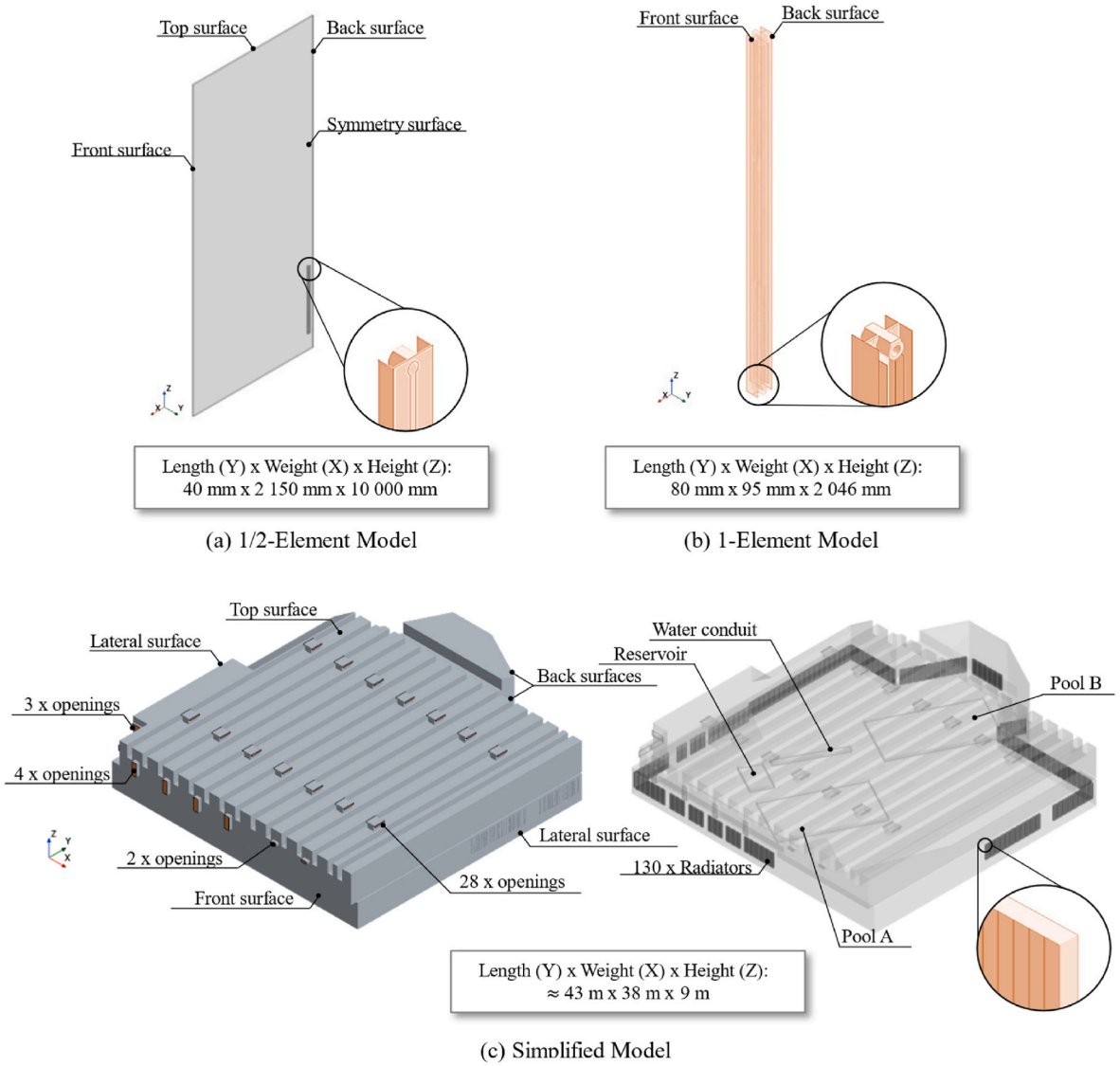

Fig. 8. Dimensions and geometrical details of the computational domains for Step 1 and Step 2.

where V_f is the volume that is occupied by the fluid, V is the total volume, $\mathbf{v}$ is the physical velocity, $\mathbf{T}$ is the stress tensor, $\mathbf{P_v}$ and $\mathbf{P_i}$ is the viscous and inertial resistance tensor, $\mathbf{v_s}$ is the superficial velocity, $\mathbf{v_s} = \chi\,\mathbf{v}$.

In summary, the implementation of the porous media required prior knowledge of several parameters: the heat transfer coefficient, h_t, the interaction area between the phases, A, the material's equivalent conductivity, k_{eq}, the water temperature profile, and the resistance of the porous media ($P_v = \mu/K_v$, $P_i = \rho/K_i$). For further details, it is advisable to refer to the referenced study [37]. Additionally, the determination of the heat transfer coefficient utilized Equation (4) in conjunction with the simulation outcomes from Step 2 employing the 1/2-Element Model in the CFD methodology. Moreover, the simplified temperature profile of the water, varying with height (coordinate z), was derived based on the inlet and outlet temperatures, expressed in Equation (5).

$$h_t = \frac{q}{A_s LMTD} \; with \; LMTD = \frac{\left(T_s - T_{air,out}\right) - \left(T_s - T_{air,in}\right)}{ln\left(\frac{\left(T_s - T_{air,out}\right)}{\left(T_s - T_{air,in}\right)}\right)} \tag{4}$$

$$T(z) = \frac{T_i - T_o}{H} \cdot z + T_o \tag{5}$$

where q is the heat flux rate, A_s is the surface contact area, LMTD is the Logarithmic Mean Temperature Difference, and z is the vertical coordinate.

5.3. Computational domain, boundary conditions and grid

This section describes the computational domains used in the two steps outlined in Fig. 7. For Step 1, the computational domains of the 1/2-Element Model and 1-Element Model were detailed in Fig. 8(a) and (b). For Step 2, the Simplified Model, representing the Roman Baths Museum with porous media, was depicted in Fig. 8(c). The dimensions of this Simplified Model were based on the Roman Baths Museum of Chaves. However, due to its large-scale nature (exceeding 10,000 m^3), certain geometric simplifications were necessary during model development.

In the model, all technical and service areas from the ground and basement floors were excluded, resulting in the consideration of only six ventilation grilles on the building facade. A consistent ceiling height was maintained throughout the building. The ventilation grilles were modelled in detail but rather treated as porous surfaces with the definition of viscous and inertial resistance coefficients (K_v and K_i). The use of this type of surface ensures the versatility of the model when conducting simulations where the opening of the grilles varies. For the Roman Baths, a value of viscous and inertial resistance coefficients (K_v and K_i) of 3.94×10^{-5} and 0.16, respectively, was considered [40]. Geometric simplifications were made to beams and other elements with multiple cutouts, and guardrails were omitted to streamline the modelling process. Radiators were placed 110 mm from the rear wall, with lower radiators at 800 mm above the floor and taller ones at 1200 mm. Air openings in the ceiling received detailed attention, with benches modelled to facilitate lateral air exhaust rather than just vertical. Regarding the pools (pool A, pool B, reservoir and water conduit), they were treated as surfaces with specific temperatures and a specific evaporation rate. Based on the ASHRAE definition [41] and the study by Smedegård, Aas, Stene and Georges, 2022 [42], the calculation of the evaporation rate considers the activity factor and is conducted using Equation (6).

$$\dot{m}_{evap} = 4 \cdot 10^{-5} \cdot A_{pool} \cdot F_{act} \cdot (p_w - p_a) \tag{6}$$

where $\dot{m}_{evap}$ is the evaporation rate [kg/s], A_{pool} is the area of pool surface [m^2], p_w is the saturation vapor pressure taken at surface water temperature [kPa], p_a is the saturation pressure at room air dew point [kPa] and F_{act} is the activity factor [−], which, in the case of the Roman Baths, is equal to 0.5, as it corresponds to the baseline (pool unoccupied) condition [41].

Considering these factors, Table 3 outlines the specific boundary conditions applied in each simulation. The Roman Baths' surroundings were treated as walls, and all exterior openings were modelled as pressure outlet conditions to ensure proper flow. The domain dimensions were approximately 43 m in length, 38 m in width, and 9 m in height. The simulation coordinate system matched the experimental reference frame, with gravitational force applied in the negative z direction at 9.81 m/s^2. Emissivity values for room walls and radiator panels were set at around 0.9 [43]. The thermal properties of materials employed in the CFD models are summarized as follows: for gases, air has a density of 1.18415 kg/m^3, dynamic viscosity of $1.86 \cdot 10^{-5}$ Pa.s, specific heat of 1003.6 J/(kg.K), and thermal conductivity of 0.03 W/(m.K). Solid materials are represented by aluminium, with a density of 2730.0 kg/m^3, specific heat of 893.0 J/(kg.K), and thermal conductivity of 163.0 W/(m.K). In the case of liquids, water has a density of 977.7 kg/m^3, dynamic viscosity of 0.0004 Pa s, specific heat of 4181.7 J/(kg.K), and thermal conductivity of 0.6 W/(m.K) [44,45].

In both stages of the methodology, an isotropic mesh with polyhedral elements was utilized to delineate control volumes, aiming to minimize the required number of elements for domain discretization. The mesh dependency study was grounded in the investigation conducted by the authors in a previous study [37], wherein the dependency was initially assessed for the 1/2-Element Model and subsequently applied to an installation with two radiators.

In the mesh study of the 1/2-Element Model, four meshes were examined: Mesh 1 (coarser), Mesh2, Mesh 3, and Mesh4 (finer), with cell sizes in the radiator region corresponding to 7.5 mm, 5 mm, 3.5 mm, and 2.5 mm, respectively. It was observed that from Mesh2 onwards, the relative error for outlet water temperature and radiator heat output fell below 0.03 % and 1 %, respectively. Two meshes, resembling the characteristics of Mesh2 and Mesh4, were generated for the model with two radiators (including all radiator details and three physics: solid, water, and air). The results revealed that when comparing outlet water temperature and radiator heat output using cells of 5 mm and 2.5 mm, with 18M cells and 58M cells, respectively, the relative error between the two meshes was below 0.5 % for both parameters. The finer mesh was deemed more accurate, and its values were used for calculating relative error. Given the reduced relative error and lower computational time, the mesh with Mesh2 characteristics was applied to the Simplified Model of the Roman Baths. Based on Mesh2, two meshes were defined for the Roman Baths: one with approximately 80M cells and another with 42M cells. Both meshes maintained the Mesh2 characteristics for porous media and inlets/outlets but varied the refinement blocks' size and direction around the radiators. The number of cells was reduced by about 48 %, significantly decreasing computation time, while the difference in radiator heat output was less than 1 %, that indicating mesh independence. The final mesh used in the simplified simulation model for the Roman Baths of Chaves is presented in Fig. 9.

5.4. Methodology implementation and model validation

In CFD, achieving simulation convergence entails overseeing residuals and observing the surface temperature of radiators/porous media and heat output. While there's no universally accepted convergence evaluation method, all simulations showed a progressive decline in residuals until stabilizing, signifying convergence. Notably, employing the unsteady-state model with a time step of 0.01 s significantly decreased residuals by 3–5 orders of magnitude.

The CFD methodology outlined in Fig. 7 involves two main steps. The first step defines a simplified numerical model, while the second step compares obtained results with experimental data. Experimental values for comparison were obtained under conditions of thermal equilibrium and correspond to identical conditions as the numerical results,

Table 3
Simulations characteristics and boundary conditions.

			1/2-Element Model	1-Element Model	Simplified Model
Radiator element	Detailed		1/2	1	–
	Simplified		–	–	1038
Materials	Gas		x	–	x
	Solid		x	x	–
	Liquid		x	–	–
	Porous media		–	–	x
Boundary conditions	Gas	Front surface	Pressure outlet	–	Wall
		Lateral surfaces	Symmetric	–	
		Other surfaces	Wall - Adiabatic	–	
		Openings	–	–	Pressure outlet (pressure jump porous)
		Pools	–	–	Wall passive scalar (specified flux)
	Solid	Front and Back surfaces	Wall	Wall - Temperature	–
		Lateral surfaces	Symmetric	Wall - Adiabatic	
		Other surfaces	Wall		
	Liquid	Inlet	Mass Flow Inlet	–	
		Outlet	Outflow	–	
	Porous media	Volume	–		Porosity Interaction area K_v, K_i
Interfaces	Gas-Solid	All surfaces	Mapped contact	–	–
	Liquid-Solid	All surfaces			
	Gas-PM	Front and Back surfaces	–		Baffle
		Other surfaces			Internal

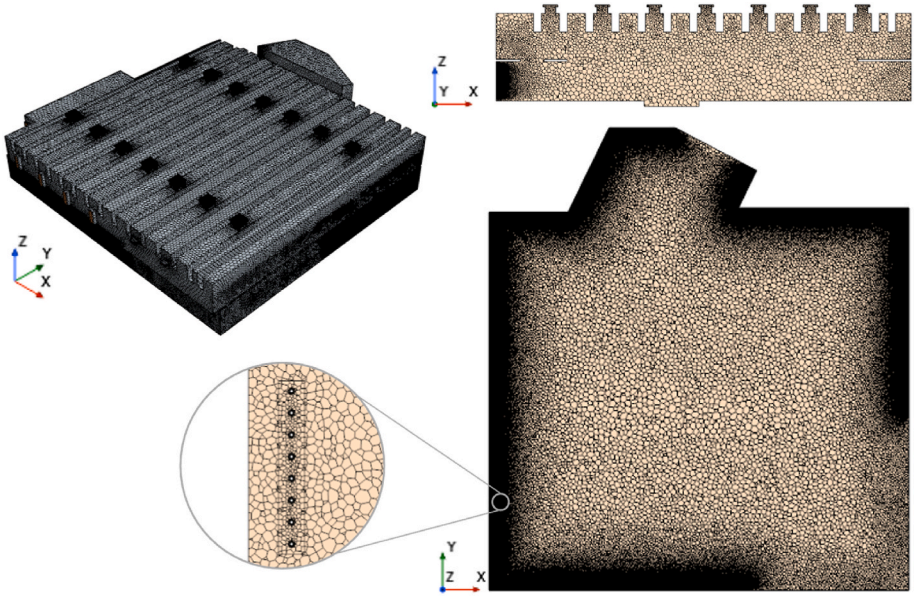

Fig. 9. Mesh of the simulation Simplified model for the Roman Baths of Chaves, providing an overview, as well as XY and XZ plane views, and a detailed view near the heat sources.

mitigating potential measurement errors. The study includes analysis of heat transfer rate and temperature at experimental planes. Resistance coefficients were determined through six simulations using the 1/2-Element Model, with varying temperature and water inlet flow rate combinations. Numerical points were plotted on a curve to calculate resistance coefficients, neglecting top effects of the radiator's geometry. When analysing data with air density at 1.2068 kg/m^3 and viscosity at 1.86×10^{-5} Pa-s, specific coefficients were derived for the radiator type: an inertial coefficient (K_i) of 2.17 and a viscous coefficient (K_v) of 1.95×10^{-3}. These coefficients indicate that flow resistance mainly stems from porous media geometry and density, rather than fluid viscosity, due to the low density of the porous media (porosity of 0.75). Detailed calculations can be found in Ref. [37]. Heat transfer coefficients (h) were calculated from six simulations (Table 4) and subsequently utilized to establish coefficients for experimental conditions. To validate the model of the Roman Baths, average values obtained from two days of testing were employed, resulting in an average water inlet temperature of 53.2 °C. This corresponds to a heat transfer coefficient of 9.2 W/m^{2}K through interpolation, at a flow rate of 0.0313 m^3/h. In the 1-Element Model simulation, the radiator's equivalent conductivity (k_{eq}) was established as 15.28 W/mK in the x-direction. Furthermore, the interaction area density was computed as 494.6/m, and the porosity of the

Table 4
Heat transfer coefficient (W/m^{2}K).

Flow rate of each element (m^3/h)	Inlet temperature (°C)		
	75	55	35
0.0313	9.4	8.4	7.1
0.0063	10.7	9.8	8.5
0.0018	12.0	11.2	10.0

porous medium was determined to be 0.75.

After determining parameters K_v, K_i, h and k_{eq}, Step 2, which involves the simplified model, commenced for the Roman Baths of Chaves. In this stage, all boundary conditions specified in Table 3 were defined. Particularly for the pool boundary conditions, the average water surface temperatures recorded during the monitoring period were considered, corresponding to 30.6 °C for Pool B and 30.6 °C for Pool A, water conduit, and reservoir, which are all at room temperature. Considering these characteristics, the respective evaporation rates were determined using Equation (6), yielding approximately 6.1×10^{-3}, 1.8×10^{-3}, 2.5×10^{-4}, and 1.7×10^{-4} kg/s for Pool B, Pool A, water conduit, and reservoir, respectively. Subsequently, after defining the entire simplified model, its simulation was initiated.

As referred to in Section 4.2, the validation of the model was conducted by comparing the experimental results presented in Table 2 with the average temperature values obtained in the simulation for the corresponding constrained planes, which correspond to the area covered by the experimentally monitored points and can be seen in Fig. 3(c). Despite the non-stationary nature of the calculation, the level of unsteadiness is very low. Therefore, all velocity and temperature fields (and others) are instantaneous fields, but very close to time-averaged fields. Based on the analysis of these results, presented in Table 5, it is observed that the relative error between the experimental data with 26 points and the CFD model results ranges between 2.0 % and 4.23 %, allowing us to conclude that the model is correctly validated since these values are much lower than the 10 % commonly used in CFD model validation for engineering purposes in complex systems.

The examination of temperature values at five specific points, as shown in Fig. 3(d), can be conducted alongside the average temperature analysis for the planes at four heights, as indicated in Table 6. The validation data for the CFD model suggests generally good accuracy, with relatively low errors at most points. At Point 1, the errors range from 4.8 % to 6.2 %, and at Point 5, from 3.9 % to 5.7 %, indicating a slight increase at the higher elevations. Point 3 shows a strong correlation, with errors between 2.2 % and 4.1 %, which may support the model's robustness. Point 2, while exhibiting slightly higher errors of 7.5 %–9.1 %, still demonstrates acceptable performance, which could be related to challenges in experimental monitoring in that area. Overall, most relative errors remain below 10 %, suggesting the CFD model's effectiveness.

Additionally, when examining scenarios with 11 and 6 experimentally monitored points (Table 2), it was observed that the relative error varied between 1.22 % to 3.70 % and 0.96 %–2.53 %, respectively. However, it's crucial to acknowledge the cumulative impact of reducing the number of monitored points on the average experimental values, as elaborated in Table 5. This cumulative effect results in a maximum relative error ranging from 2.07 % to 4.21 %. This underscores the importance of employing a minimal number of experimentally monitored points to effectively validate the model, as previously suggested in Section 4.2 for large naturally ventilated spaces.

Table 5
Relative errors from the CFD model validation of average temperatures at four heights (z).

		Planes			
		z = 1m	z = 2m	z = 3m	z = 4m
CFD temperatures [°C]		22.8	23.4	23.7	24.0
RE [%] [a]	**28 points**	2.08	3.05	4.02	4.23
	11 points	1.22	2.28	3.37	3.70
	6 points	0.96	1.96	2.97	2.53
Cumulative RE [%] [b]	**11 points**	2.07	3.03	4.00	4.21
	6 points	2.07	3.03	3.99	4.19

[a] RE is the relative error considering the data from the 26 points as the most accurate value.

[b] Cumulative RE is the sum of the relative errors compared to the CFD data and the number of experimental points to determine the plane average, as shown in Table 2.

Table 6
Relative errors from the CFD model validation of temperatures at five specific points and four heights (z). For the location of the points, see Fig. 3 (d).

Points		Planes			
		z = 1m	z = 2m	z = 3m	z = 4m
1	Experimental	22.3	22.6	22.8	23.0
	CFD	23.4	23.7	24.0	24.5
	RE (%)[a]	4.8	4.9	5.3	6.2
2	Experimental	22.0	22.4	22.3	22.3
	CFD	23.7	24.0	24.2	24.3
	RE (%)[a]	7.5	7.5	8.6	9.1
3	Experimental	22.8	23.2	23.1	23.1
	CFD	23.6	23.7	23.8	24.0
	RE (%)[a]	3.5	2.2	2.9	4.1
4	Experimental	22.6	22.8	22.8	23.2
	CFD	23.4	23.6	23.9	24.2
	RE (%)[a]	3.8	3.4	4.7	4.2
5	Experimental	22.2	22.6	22.6	23.0
	CFD	23.1	23.5	23.9	24.4
	RE (%)[a]	3.9	4.1	5.7	5.7

[a] RE is the relative error considering the experimental data as the most accurate value.

In line with the proposal for large naturally ventilated spaces, validating the CFD model necessitates monitoring experimentally defined test points arranged in a 3 × 3 matrix. This involves selecting the primary area of the space and positioning points at the four corners of each side, as well as the central point. Additionally, supplementary points should be placed in areas that deviate from the square geometry of the space, at four heights within the space.

It is important to note that the validation was based on temperature parameters, as the monitored velocities on the basement floor recorded average values below 0.06 m/s at heights of 1, 2, 3, and 4 m. According to the accuracy of the measurement equipment, this is effectively considered 0 m/s, making it unfeasible to use this data for model validation, which is characteristic of naturally ventilated spaces [29]. Additionally, relative humidity was used as a parameter for model validation, with measurements taken at specified points, as shown in Fig. 3(a).

This section also covered the simplification of pools in the CFD model. As previous outlined, pools were modelled with passive scalar wall boundary conditions, specifying their temperature and evaporation rate (Equation (6)). To validate this simplification, we analysed planes that intersected the pool at x = 14.5m and y = 16.8m (see Fig. 3(d)). The analysis considers the passive scalar, representing the concentration of water vapor in kg/m^3, accounting for the flux imposed in the boundary condition. However, for a more comprehensive analysis and to complement the model validation, this quantity was reflected in terms of relative humidity, RH [%] (Equation (7)), through the application of psychrometric equations [46].

$$RH = \frac{p_s}{p_{ws}} \tag{7}$$

where p_s is the vapor pressure [kPa], given by Equation (8), and p_{ws} is the saturation vapor pressure [kPa], given by Equation (9).

$$\ln(p_{ws}) = \frac{C_1}{T} + C_2 + C_3 T + C_4 T^2 + C_5 T^3 + C_6 T^4 + C_7 \ln(T) \tag{8}$$

where T is the air temperature [K] and the constants are: $C_1 = -5.8002206 \times 10^3$, $C_2 = 1.3914993$, $C_3 = -4.8640239 \times 10^{-2}$, $C_4 = 4.1764768 \times 10^{-5}$, $C_5 = -1.4452093 \times 10^{-8}$, $C_6 = 0$, and $C_7 = 6.5459673$.

$$p_s = \frac{C \times R \times T}{M} \tag{9}$$

where C is the concentration of water vapor [kg/m^3], R is the ideal gas constant (8.314 J/(molK)), and M is the molar mass of water (18.015 g/mol).

Through the analysis of Fig. 10, it is evident that the relative humidity serves as a crucial complementary parameter for validating the model. The highest relative humidity value occurs in the area above Pool B (see Fig. 3(d)), reaching approximately 70 %, which is expected due to its larger area and higher water temperature compared to the other pools. As anticipated, this maximum value surpasses the experimentally recorded relative humidity at point C1 during the control test, which is the closest point to Pool B. The average relative humidity over the two test days, around 66 %, further supports the consistency between numerical predictions and experimental results. These findings not only validate the numerical simulations but also highlight the significant impact of pool characteristics on indoor humidity levels.

Moreover, a detailed examination of Fig. 10(a) reveals a notable decrease in relative humidity with increasing building height (z-direction), showing a reduction of about 10 % between the z = 1 m and z = 6 m planes above the four pools. Fig. 10(b) and (c) provide further evidence of these trends, clearly illustrating the differences in relative humidity between Pool B and Pool A (as shown in Fig. 3 (d)). This contrast is particularly influenced by the surface temperatures of the pools, with Pool B reaching approximately 31 °C and Pool A maintaining around 22 °C. In summary, while areas with relatively high humidity levels (above 60 %) have been identified, the average relative humidity within the thermal baths typically ranges from 25 % to 40 %. These lower humidity levels can be attributed to the heat sources and natural ventilation facilitated by the designed system, which effectively addresses the humidity issues identified during the initial phases of the Roman Baths museum's rehabilitation [10].

6. Natural ventilation performance

After validating the model, the objective was to explore its potential for assessing ventilation performance across various scenarios where operational conditions vary. The analysis includes scenarios considering two different operating conditions, referred to as experimental and design. These terms are used to distinguish the specific parameters for each scenario, but they simply represent different points of operation for the installation. For design conditions, the temperatures for the outdoor air, the radiators' inlet, Pool A, Pool B, water conduit, and reservoir are 9.4, 55, 20, 36, 44, and 48 °C, respectively, while for experimental conditions, these temperatures are 12.0, 53, 22, 31, 22, and 22 °C, respectively.

Evaluating ventilation performance in large space naturally ventilated poses challenges due to air distribution patterns, so the goal is to

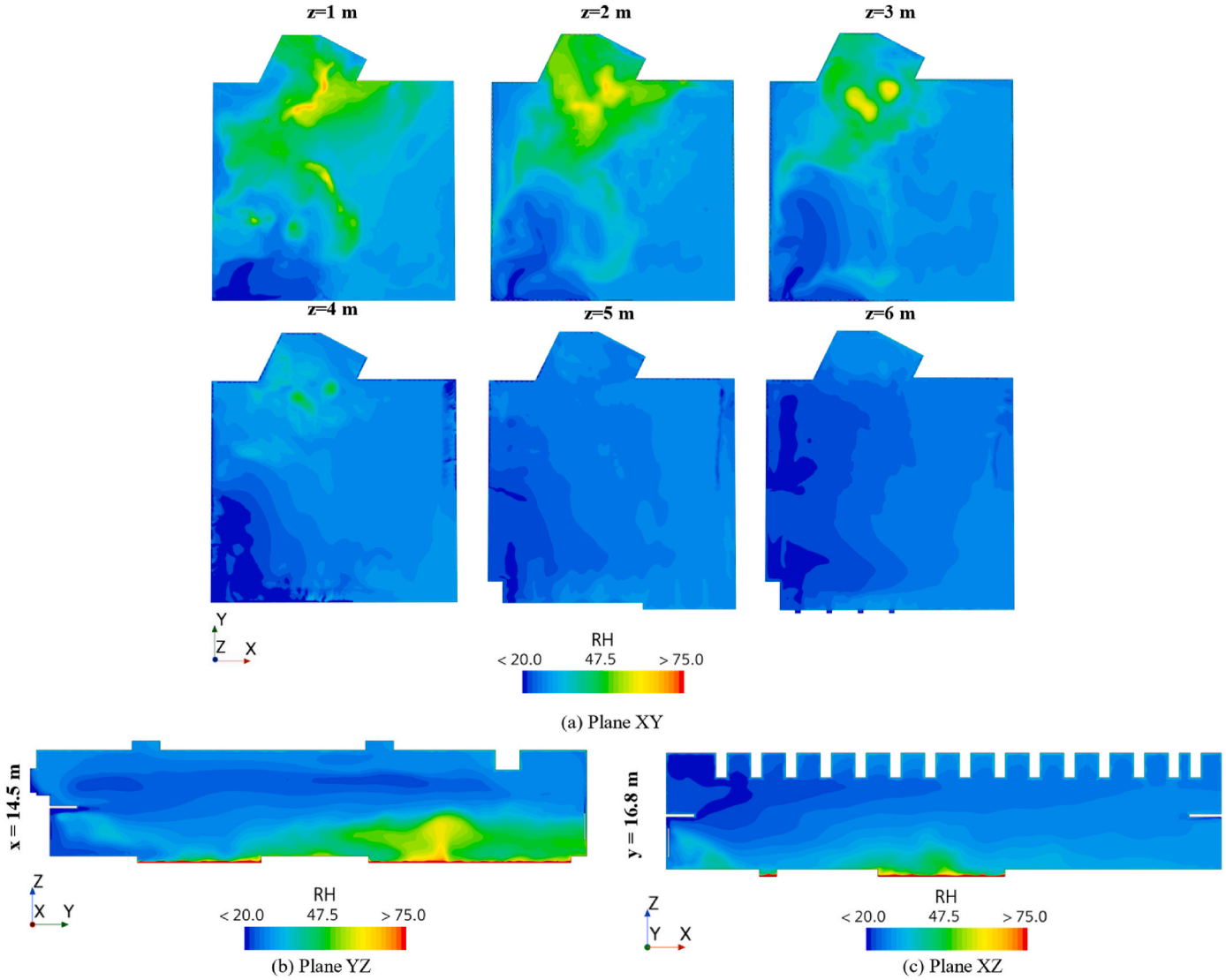

Fig. 10. Relative humidity maps resulting from the contribution of pools in the simplified model of the Roman Baths.

verify if performance can be coherently assessed both qualitatively and quantitatively through four distinct methods: analysis of Air changes per hour (ACH), application of the Richardson number in two variants, analysis of vertical temperature and velocity profiles, and examination of temperature and velocity contour maps, including a statistical analysis of the map data. These analyses are based on the numerical results presented in Figs. 10–15, which indicate an average indoor temperature of approximately 24.8 °C and a radiators power of about 124 kW for the experimental conditions, and around 24.7 °C and 115 kW for the design conditions.

Air changes per hour are typically used to evaluate ventilation performance, with the calculation based on airflow rates at the outlets. The experimental conditions showed an air change rate of 2.4 ACH, compared to 2.2 ACH for the design conditions, indicating a higher renewal rate under experimental conditions. Both conditions meet the minimum legislative requirement of 0.54 ACH [10], yet this assessment does not provide insight into the efficiency of air distribution within the space.

Literature review identified the use of the Richardson number (Ri) to estimate the ratio of buoyancy to inertial forces influencing natural ventilation [47–50]. When Ri $\ll$ 1, forced convection prevails; conversely, when Ri $\gg$ 1, natural convection dominates. At Ri = 1, both convection effects exhibit equal intensity. The Richardson number is defined as the ratio of the Grashof number (*Gr*) to the square of the Reynolds number (Re) [47–50]. The Richardson number is estimated according to Equation (10).

$$Ri = \frac{g\,\beta\,(T_i - T_o)H}{u^2} \tag{10}$$

where g is the gravity [m/s^2], β is the thermal expansion coefficient [1/K], u is the average internal velocity [m/s], and T_i is the average internal temperature [°C], H is the characteristic height of the space [m] and T_o is the outdoor temperature [°C].

In the present study, experimental conditions yielded a Richardson number (Ri) of 197.3, while for design conditions, Ri was 241.3. Initially, as both Ri values are significantly greater than 1, it can be observed that natural convection dominates, as Richardson number is an indicator of the predominance of buoyancy over inertia in an airflow. However, when Ri values are in the very high range, this suggests that buoyancy effects are extremely dominant. Nevertheless, for efficient

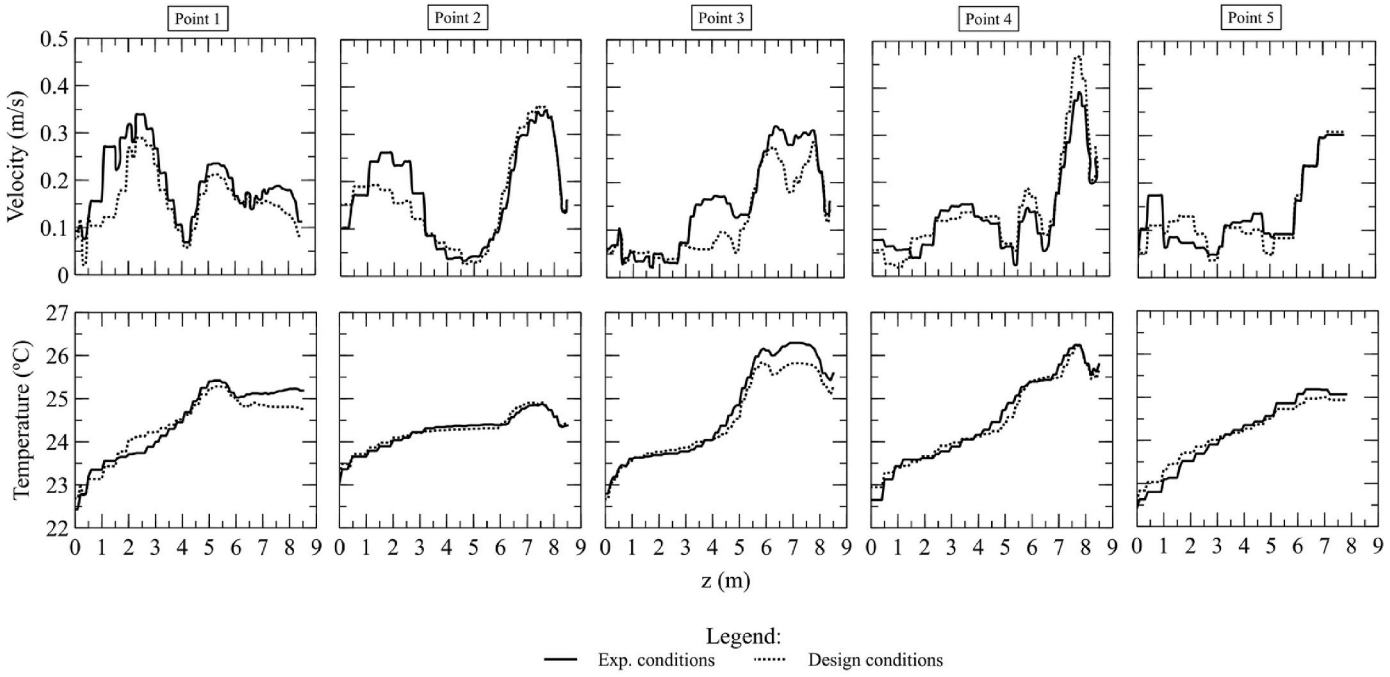

(a) Evolution of temperature and velocity at each point

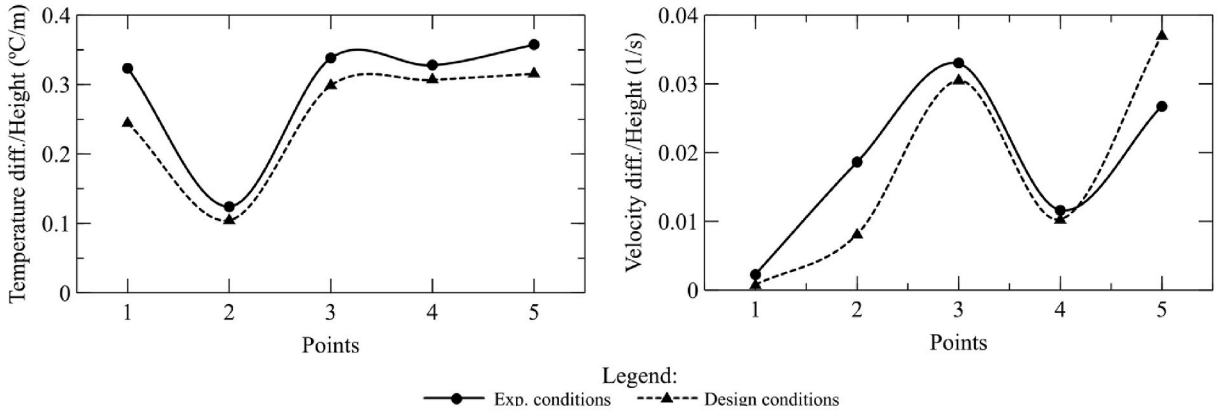

(b) Temperature and velocity ratios for each point

Fig. 11. Analysis of stratification, through profiles for 5 points located according Fig. 3(d).

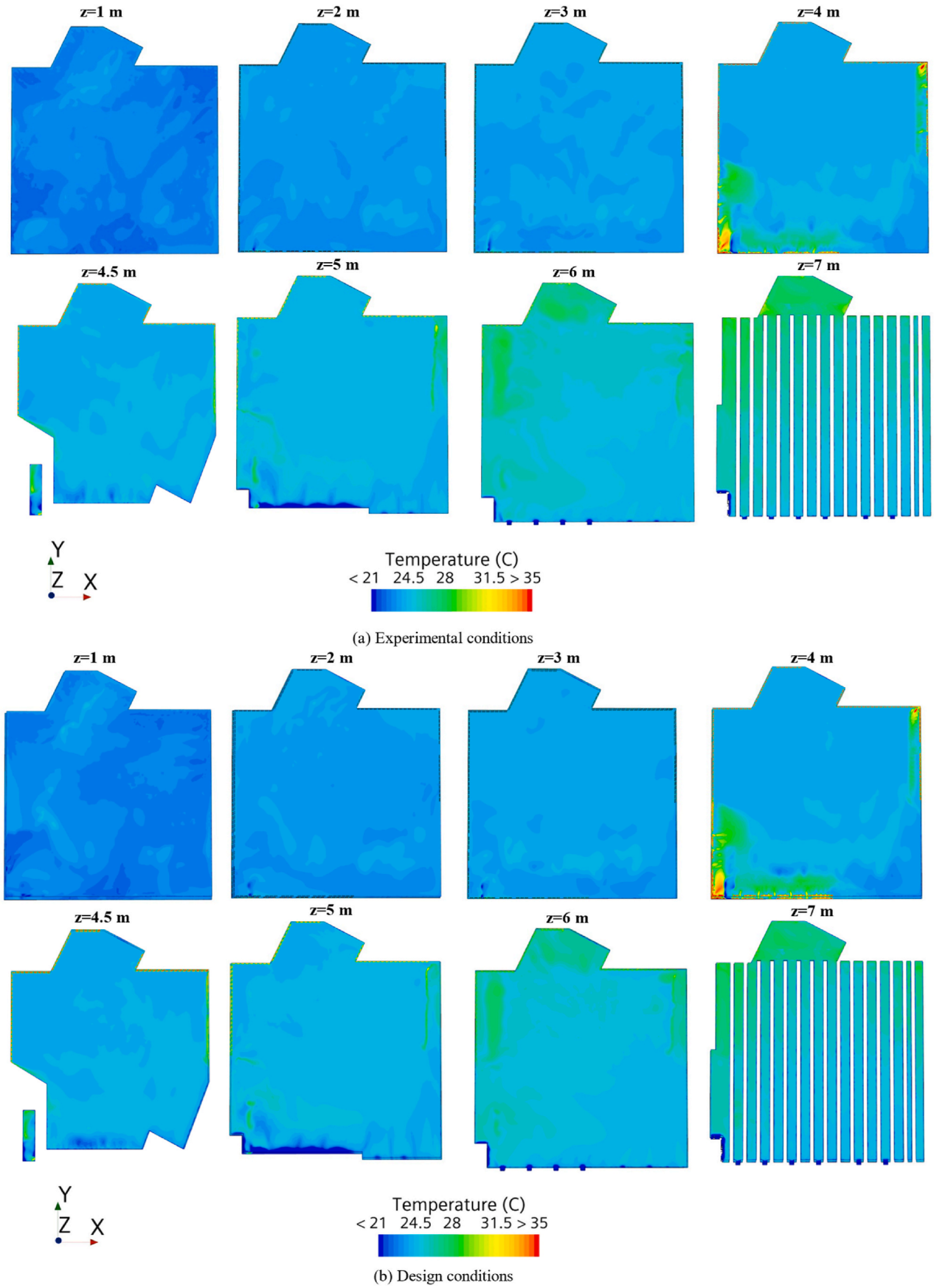

Fig. 12. Temperature maps in the XY plane for different heights inside the Roman Baths.

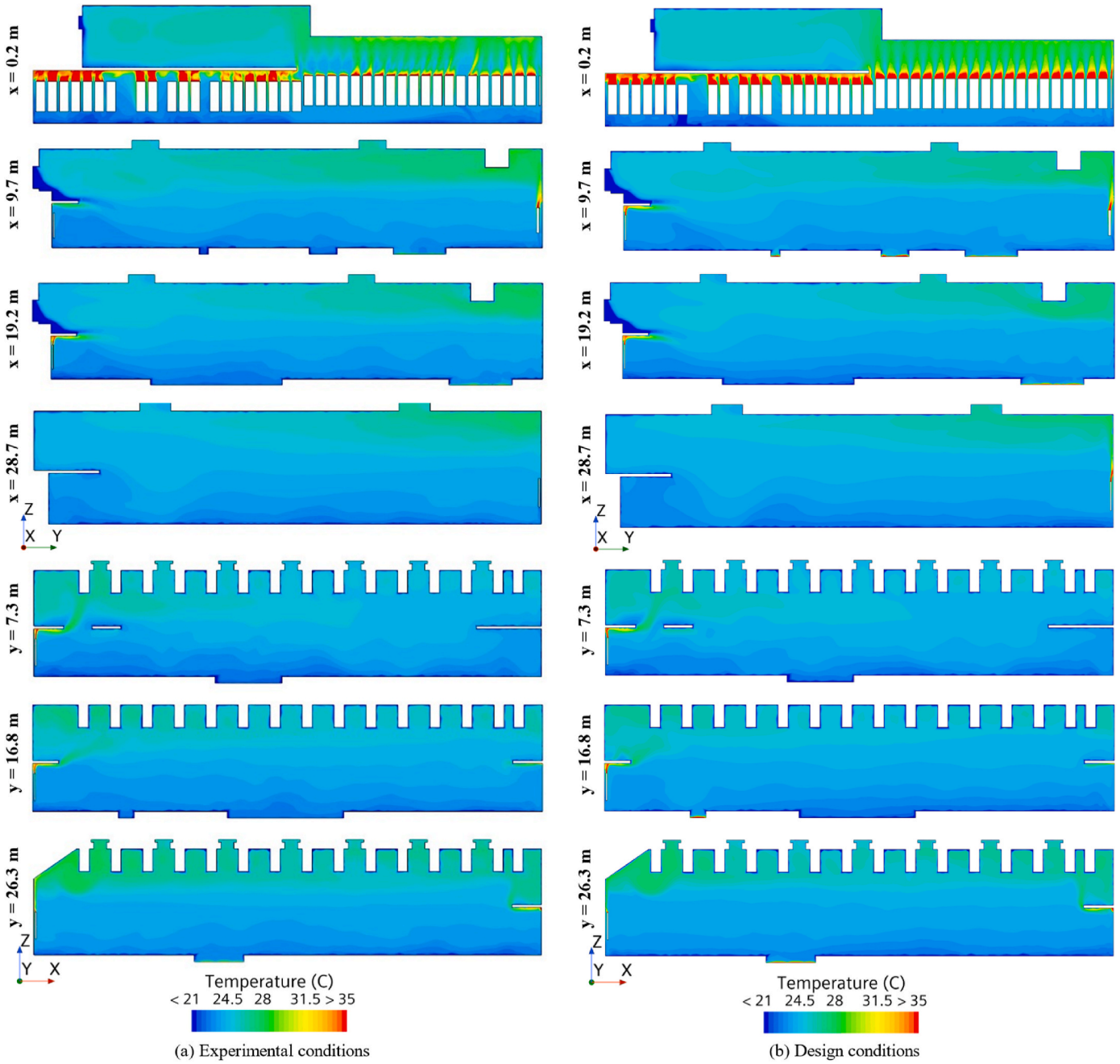

Fig. 13. Temperature maps in the YZ and XZ planes (see Fig. 3(d)).

natural ventilation, a balance between buoyancy and inertia is desirable. Very high Richardson numbers indicate that the flow is strongly influenced by thermal stratification, which may result in less mixing and, consequently, less effective ventilation. Upon direct analysis, both conditions result in high Ri values, yet for experimental conditions, the value is approximately 20 % lower, suggesting a slightly better contribution of inertia compared to design conditions. Therefore, experimental conditions may lead to slightly better natural ventilation than design conditions because the lesser dominance of buoyancy will allow for a bit more mixing and air movement. These values are in the same order of magnitude as those determined in the boiler house study [47], where Ri was 121.5. According to the authors, this value suggested that the specified operational conditions for the aviary produced a dominance of thermal buoyancy that could be affecting internal airflow. However, they did not comparatively determine this to other ventilation scenarios.

So, Ri was calculated based on indoor velocity and indoor temperature, this number has been considered in the literature taking into account the surface temperature of heat sources and the outdoor velocity, according to Equation (11) [48,49]. According to study [49], at Ri > 1.6, the flow in and around the downstream workshop changes from wind-driven to buoyancy-driven. The indoor pollutant concentration reaches a steady state for Ri = 4.8.

$$Ri = \frac{g\,\beta\,(T_w - T_{ref})H}{U_{ref}^2} \tag{11}$$

where T_w represents the surface temperature of the heat source in the downstream workshop, T_{ref} is the reference temperature of the outdoor air, and U_{ref} is the reference wind speed, parameterized with a value of 1.7 m/s according to the annual average wind speed in Chaves [51].

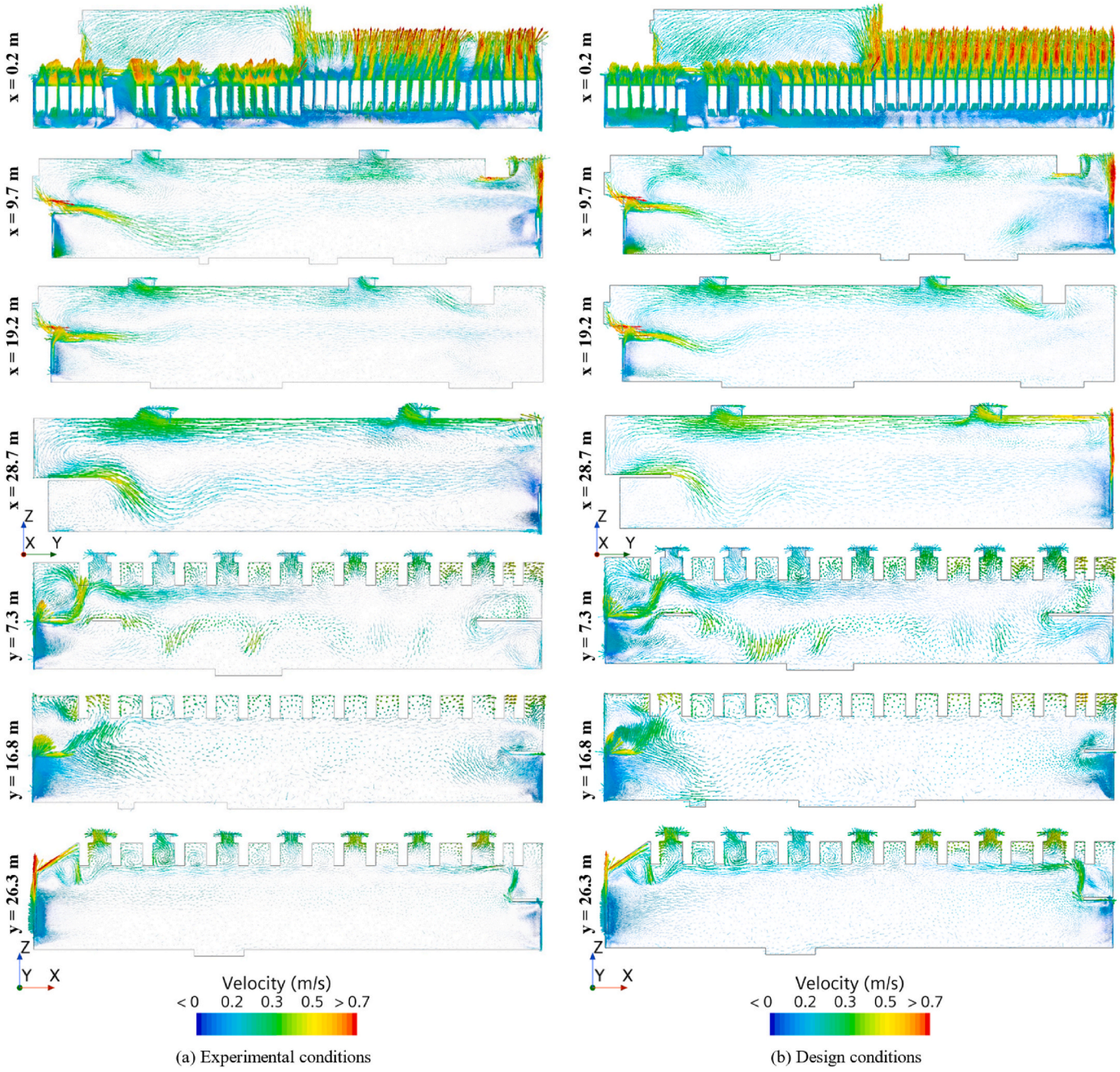

Fig. 14. Velocity vector maps in the YZ and XZ planes (see Fig. 3(d)).

The analysis between experimental and design conditions reveals a difference in the Richardson numbers (Ri) obtained from Equation (11), with values of 2.7 and 2.4, respectively. This approximately 9 % variation in Ri can be justified by considering more extreme conditions during the design phase. Specifically, a lower Ri in the design (2.4) compared to the experimental value (2.7) suggests that the design accounts for scenarios with less buoyancy dominance and a greater relative influence of inertial forces, such as winds or additional air movements. This adjustment is typical in designs that need to ensure ventilation effectiveness across a wider range of operational conditions, including those with lower outdoor temperatures and higher pool water temperatures, which may intensify the impact of inertial forces. In this interpretation, it means that ventilation corresponding to experimental test conditions performs slightly better than for design conditions, corroborating the analysis and interpretation of indoor conditions through the determination of Ri based on Equation (10). Additionally, these conditions correspond to the case with higher ACH.

Considered profiles in the z-direction for points 1 to 5, as depicted in Fig. 3(d). The selected profiles for analysis were based on the method proposed to validate the model, for the case with the fewest number of points. These profiles encompass points throughout the height of the Roman Baths. The profiles are presented in Fig. 11(a) and allow for quantitative evaluation of stratification, and consequently, air distribution within the space. Comparing the profiles reveals that the evolution of both temperature and velocity at the 5 points is similar for both experimental and design conditions; however, the greatest differences were recorded for temperature profiles at points 1 to 3. Nonetheless, variations were observed in the absolute values of temperature and velocity. To quantify the stratification between conditions, the ratio of the temperature or velocity difference between the highest and lowest

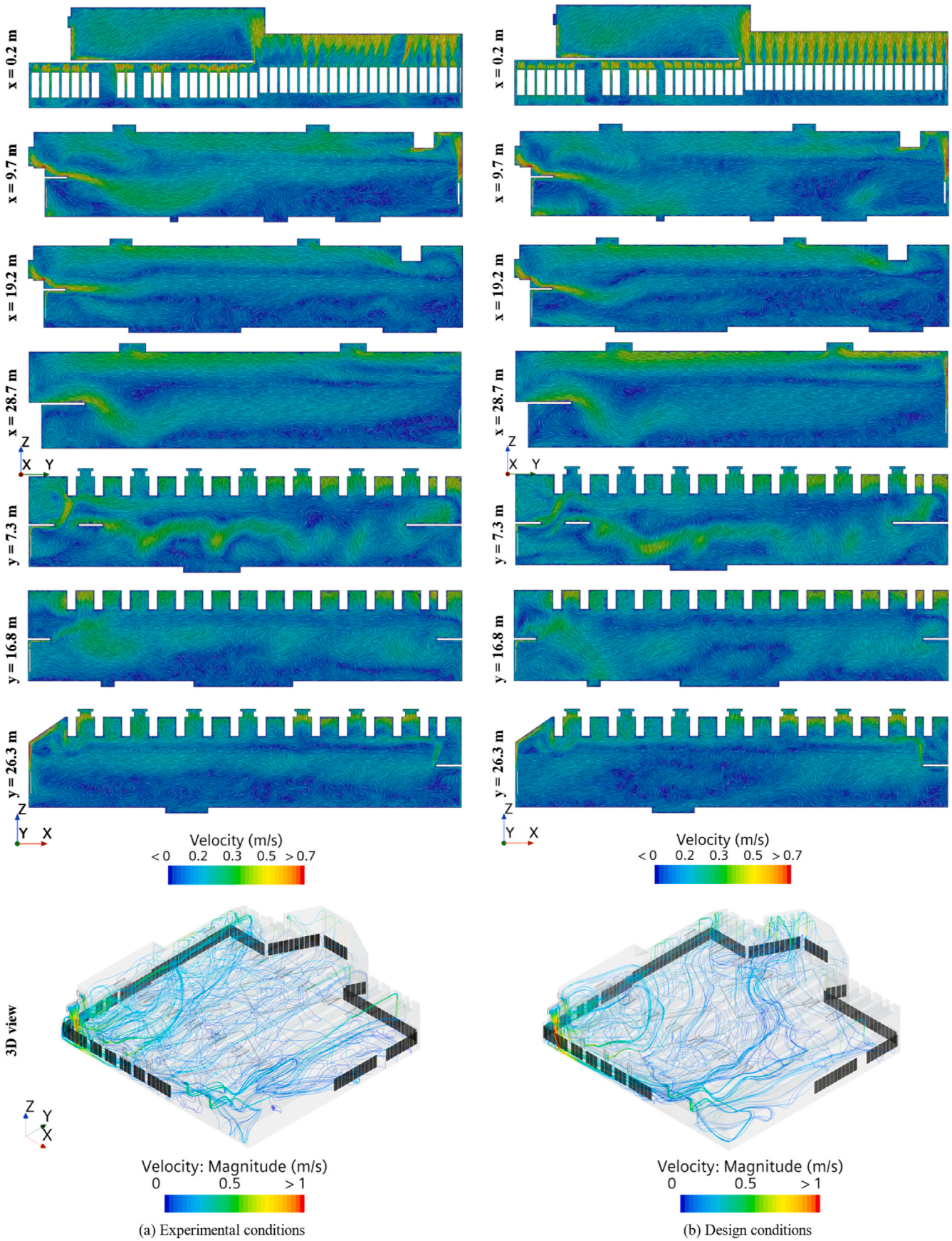

Fig. 15. Velocity maps with contour lines and velocity streamlines (see Fig. 3(d)).

points in the z-direction to the total height of the Roman Baths building was determined. These ratios for each point are presented in Fig. 11(b). The figure shows the temperature and velocity differences across the entire height, from top to bottom, at each point. For temperature in experimental conditions, the $\Delta T/H$ ratio was 0.32, 0.12, 0.34, 0.33, and 0.36 for points 1 to 5, respectively, and for design conditions, it was 0.24, 0.10, 0.30, 0.31, and 0.32 for points 1 to 5, respectively. Analysis of these results indicates that for experimental conditions, the ratios range from 0.12 to 0.36. Point 2 has the lowest ratio (0.12), indicating a lesser temperature difference along the height at that specific point. Points 1, 3, 4, and 5 have ratios above 0.3, suggesting greater stratification. For design conditions, the ratios range from 0.10 to 0.32. Similarly, point 2 has the lowest ratio (0.10). The other points have ratios above 0.2, with the highest value being 0.32 at point 5. Comparing experimental and design conditions, it is observed that at points 1 and 2, the experimental condition exhibits greater stratification compared to the design condition, with values of 0.32 versus 0.24 at point 1 and 0.12 versus 0.10 at point 2, with the difference being more pronounced at point 1. At points 3 to 5, the experimental and design conditions display similar stratification values; however, the experimental condition generally has slightly higher values, suggesting slightly greater stratification. Upon further analysis, point 2 exhibits the least stratification in both conditions, indicating that this location is associated with an area of the building where temperature is more uniformly distributed vertically due to reduced influence from heat sources and building openings. Overall, the experimental condition tends to show greater stratification compared to the design condition, possibly because real conditions incorporate factors that increase vertical temperature variation.

For velocity, in experimental conditions, the $\Delta u/H$ ratio was 0.0023, 0.0186, 0.0330, 0.0116, and 0.0267 for points 1 to 5, respectively, and for design conditions it was 0.0007, 0.0080, 0.0305, 0.0102, and 0.0370, respectively. Analysis of these results indicates that for experimental conditions, the ratios range from 0.0023 to 0.0330. Point 1 has the lowest ratio (0.0023), indicating minimal velocity difference along the height. Point 3 has the highest ratio (0.0330), suggesting greater stratification. For design conditions, the ratios range from 0.0007 to 0.0370. Point 1 again shows the lowest ratio (0.0007), while point 5 has the highest ratio (0.0370), suggesting greater velocity stratification at this specific point under design conditions. When comparing velocity ratios between experimental and design conditions, there is variation in values at different points. At points 1 and 2, the experimental condition exhibits higher ratios compared to the design condition, being 0.0023 versus 0.0007 at point 1 and 0.0186 versus 0.0080 at point 2, indicating greater vertical air velocity variation under experimental conditions, with the difference being more pronounced at point 2. At points 3 to 5, the values are closer between conditions, with the experimental condition showing a slightly higher ratio at point 3 (0.0330 vs 0.0305) and point 4 (0.0116 vs 0.0102), while at point 5, the design condition has a higher value (0.0370 vs 0.0267), suggesting greater air velocity stratification at this point. Upon closer analysis, point 1 shows the lowest ratio in both conditions, indicating less vertical variation in air velocity at this point, reflecting a more uniform distribution. However, point 5 under design conditions exhibits the highest ratio, suggesting greater vertical variation in air velocity, possibly due to specific design factors not replicated in the experimental condition. Overall, the experimental condition tends to show higher air velocity ratios.

To further understand the variability in temperature and velocity, the standard deviations at different heights were also analysed. For temperature, the standard deviations at Point 1 were 0.83 for experimental and 0.72 for design conditions, indicating greater variability in the experimental condition. At Point 2, the deviations were 0.39 and 0.38, respectively, showing little difference. Point 3 had deviations of 1.13 (experimental) and 0.95 (design), Point 4 had 1.03 (experimental) and 0.96 (design), and Point 5 had 0.83 (experimental) and 0.67 (design), all indicating higher variability in the experimental condition. For velocity, the standard deviations were similar across conditions at most points: 0.07 and 0.06 at Point 1, 0.10 for both at Point 2, 0.10 and 0.08 at Point 3, 0.09 and 0.11 at Point 4, and 0.08 for both at Point 5. This suggests that while the temperature variability is generally higher in experimental conditions, the velocity variability is more consistently replicated in the design model.

With these results, it can be concluded that experimental conditions reveal greater stratification for both temperature and velocity parameters, while design conditions exhibit stratification of lesser magnitude. Although capturing the general trends, design conditions possibly represent more extreme conditions than experimental conditions.

From a qualitative perspective, and to consider air distribution patterns, contour maps for temperature are analysed in XY planes (Fig. 12) and in YZ and XZ planes (Fig. 13), to visualize temperature distribution at different heights, and vector maps in YZ and XZ planes (Fig. 14), to observe air flow direction and magnitude. The XY planes were defined to correspond to the experimental planes, while the remaining ones cover the entire height of the Roman Baths. The YZ and XZ planes were defined according to the specifications in Fig. 3(d), considering the definition of the experimental point mesh.

Analysing stratification for experimental conditions (Fig. 12(a)), it is observed that temperature distribution remains relatively uniform up to a height of 3 m (z level). At this height, thermal exchange and air circulation appear to be efficient, resulting in minimal vertical temperature variation. However, above 3 m, an increase in temperature range is noted, particularly near the heat sources. This pattern suggests that thermal plumes generated by the heat sources do not disperse evenly, leading to local temperature elevation and consequently, greater thermal stratification in those areas. Specifically, at a height of 4 m, temperature distribution becomes less uniform. At this level, which corresponds to the plane immediately below visitor circulation zones, temperature variation is pronounced, with areas registering temperatures above 35 °C. These regions correspond to locations where thermal plumes must contend with circulation zones, resulting in a concentration of heat that increases stratification. In contrast, temperatures near building openings are below 21 °C.

Comparing with design conditions (Fig. 12(b)), it is observed that, despite a general similarity in temperature distribution patterns, there are differences in stratification. At heights of 1 m, design conditions show more evident variations due to different pool temperatures, creating temperature gradients that impact stratification at this level. These gradients reflect the direct influence of pools on thermal distribution, generating areas of non-uniform temperature that contribute to stratification. Additionally, at heights of 4 m and 5 m, the thermal influence of the pools, particularly Pool B, results in higher average temperatures, affecting stratification.

Stratification in experimental conditions proves to be more pronounced compared to design conditions, as temperature maps of design conditions exhibit smoother transitions between heights and the gradient between the 1m and 5m plane is smaller.

Fig. 13 allows identification of distinct temperature layers indicating the presence of stratification for both experimental and design conditions in both x and y directions. In these planes, the effect of the thermal plume contour of the heat sources in relation to circulation zones is visible, plane x = 19.2 m and plane y = 7.3 m. Furthermore, at y = 26.3 m plane, the effect of the plume contour on a geometric element of the roof is also visible. In these profiles, continuous layers can be identified at lower heights (up to 3m), corroborating the previous analysis, and observing the effect of heat sources and geometric elements on stratification. Comparing the two conditions, similar patterns are visible, the height of the layers is identical. The major difference is observed for the x = 0.2 m plane that intersects the heat sources, as in this plane, the thermal plumes from the heat sources are more pronounced given the initial difference between the conditions. Also, for these planes, smoother transitions between identified layers and a smaller temperature gradient are visible, for the case of design conditions compared to experimental conditions, being more noticeable in the y = 26.3 m plane.

To analyse air distribution, velocity vector maps (Fig. 14) and velocity maps with contour lines (Fig. 15) were observed to identify recirculation regions and airflow distribution patterns. In Fig. 14, it can be observed that fresh air intake occurs laterally, moving downward to circumvent the circulation regions' floor (Plane x = 9.7 m and x = 28.7 m). Near the radiators (plane x = 0.2 m and plane y = 26.3 m), heated air follows an upward trajectory towards the roof, circumventing the different geometric elements of the building. At the outlets located in the roof (plane y = 7.3 m and y = 26.3 m), heated air is expelled from the thermal baths, following a trajectory that circumvents the various beams, with each trajectory following an upward path and finally exiting to both sides. In the region of the thermal baths less affected by heat sources, velocity magnitudes are lower, and the patterns are less directional. The velocity magnitude varies in different parts of the environment. Higher magnitudes were recorded in regions near the radiators, followed by regions near the outlets, while reduced speeds are observed in regions near the entrances. In summary, ascending patterns are observed for both conditions in the radiator region, and despite ascending patterns, they circumvent the geometric elements above the radiators. Near the lateral openings, descending patterns can be identified, and in the region of the roof outlets, horizontal flows can be observed on both sides of the outlet openings. In the centre of the environment, flow patterns are smoother and less directional as the air mixes with the internal environment, resulting in a more uniform temperature distribution. When comparing the two conditions, it is noted that velocity magnitudes are slightly lower in the design conditions compared to the experimental conditions. This suggests that despite similar flow patterns, the ventilation system in the design conditions may have slightly lower efficiency in terms of air velocity.

In Fig. 15, velocity maps with contour lines are presented to provide a detailed representation of velocity distribution for both conditions. While colours indicate velocity magnitude, contour lines help visualize where velocity values change and how this change occurs in the planes.

Across various planes, several regions can be observed where contour lines form a circular or closed pattern, indicating potential recirculation zones, with particular emphasis on planes y = 7.3 m and y = 26.3 m. These regions are mostly located between the roof beams and in the upper opening regions, as well as above circulation zones. Identifying these recirculation zones is important as they can affect ventilation performance and consequently thermal comfort and indoor air quality. In the centre of the environment, where air velocity contour lines show a more diffuse and less directional flow pattern, there is greater mixing between air currents. This results in a more uniform temperature distribution throughout the environment. When the flow pattern is smoother and less directed, different air currents mix more efficiently, reducing significant temperature variations in different areas of the environment.

When comparing the design conditions with the experimental ones, lower velocities and a lower density of velocity contour lines are observed, especially notable in the plane where x = 19.2 m and y = 26.3 m. The lower density of contour lines indicates a less uniform or directional distribution of airflow, leading to less effective air mixing within the space, as analysed earlier.

Finally, also in Fig. 15 3D view of the velocity streamlines inside the thermal model for both conditions is presented, reflecting the analysis in the 2D planes.

The qualitative analysis of the previous temperature and velocity maps is supported by a statistical analysis that includes matrix data on the differences in temperatures and velocities between the experimental and design conditions for all points in the YZ and XZ planes. For planes with significant differences, the x = 19.20 m plane shows an average temperature difference of 0.16 °C, indicating that the design condition scenario has higher temperatures, while the x = 28.70 m plane shows an average difference of −0.37 °C, indicating significantly lower temperatures in the experimental condition scenario. Conversely, in planes with smaller differences, such as x = 0.20 m (−0.03 °C), x = 9.70 m (−0.20 °C), y = 16.80 m (−0.14 °C), y = 26.30 m (0.14 °C), and y = 7.30 m (0.06 °C), the variations are less pronounced.

Beyond temperature differences, it is interesting to group the data by planes, such as YZ and XZ planes, to identify general trends in velocity differences. For the YZ planes, the average velocity differences range from 0.005 m/s to −0.021 m/s, while for the XZ planes, the averages range from −0.004 m/s to 0.014 m/s. These differences suggest that, in some categories, the experimental condition scenario has lower velocities, indicating variations in flow conditions.

Regarding variability, the standard deviation of the temperature difference reveals a diverse range, with the x = 0.20 m plane showing a high standard deviation of 2.09 °C and the y = 16.80 m plane exhibiting a low of 0.43 °C. This indicates a dynamic range of temperature differences, particularly for the x = 0.20 m plane. When analysing velocity, the standard deviations ranging from 0.05 to 0.09, suggesting that velocity differences are consistently stable and exhibit less variation compared to temperature differences.

These statistical data suggest that the planes x = 19.2 m and x = 28.7 m show notable temperature variations between the scenarios. This finding aligns with the qualitative analysis, which identifies distinct temperature layers and indicates stratification in both x and y directions. Planes with smaller differences, such as x = 0.2 m and y = 16.8 m, suggest a less pronounced influence of heat sources and geometric elements, supporting the qualitative observation of continuous layers at lower heights (up to 3 m). Additionally, the statistical data indicate that in planes like x = 0.2 m, the average temperature difference is relatively small, which corresponds with the qualitative analysis where stratification patterns are more subtle.

After a comprehensive analysis of the four methods for evaluating natural ventilation performance, it is evident that they have converged to consistent results. Although a slight improvement was observed in the experimental conditions compared to the design ones, natural ventilation was effectively indicated as a viable solution. The use of these four methods has proven to be sufficient for analysing ventilation performance in large naturally ventilated spaces. Additionally, it is important to highlight that the model was validated with a significantly reduced number of experimental points, suggesting its robustness and effectiveness in predicting ventilation performance in different contexts.

7. Conclusions

The study successfully validated a CFD model for large spaces using experimental data from the Roman Baths Museum in Chaves, Portugal. Sensitivity analysis determined the optimal number of monitoring points required for accurate model validation, establishing benchmarks that serve as inputs to assist in decision-making for validating models in extensive volumes, particularly where monitoring equipment is limited. The validated model assessed ventilation performance under various operational scenarios, addressing challenges in evaluating complex air distribution patterns in large spaces naturally ventilated.

The CFD model validation analysed temperature data from four planes and conducted a sensitivity analysis to determine the required number of monitoring points for accurate validation in large volumes. Three scenarios were considered: using all 26 points, 11 points in a 3 × 3 grid with additional extreme points, and 6 points in a cross pattern. Results showed low relative errors (0.5 %–0.8 % for 11 points and 1 %–1.75 % for 6 points) compared to the full 26-point scenario, suggesting consistent temperature variations. Validation involved comparing experimental data with simulated average temperatures, with relative errors ranging from 2.0 % to 4.23 % for the 26-point scenario, below the 10 % validation threshold. Additionally, scenarios with 11 and 6 experimentally monitored points showed relative errors ranging from 2.07 % to 4.21 %. This highlights the feasibility of employing a minimal number of experimentally monitored points for effective model validation, following a predefined test point arrangement in a 3× 3 matrix. Supplementary points should be strategically placed to cover deviations

from the square geometry of the space.

The validated model explores ventilation performance in varying operational scenarios, analysing experimental and design conditions with different outdoor temperatures and internal factors like radiators and pools. Four methods were used to evaluate ventilation: air changes per hour, Richardson number variants, vertical temperature/velocity profiles, and temperature/velocity contour maps.

Experimental conditions showed an air change rate of 2.4 ACH, while design conditions had a rate of 2.2 ACH, suggesting that ACH may not be the most effective metric for performance evaluation, given the minimal difference (0.2 ACH). Richardson numbers showed that experimental conditions had a lower value (197.3) compared to design conditions (241.3), suggesting less dominance of buoyancy and slightly better natural ventilation. The analysis indicates that experimental conditions may lead to slightly better ventilation due to a lesser dominance of buoyancy, allowing for more mixing and air movement. This interpretation is supported by the difference in Richardson numbers between experimental and design conditions. These findings suggest that the ventilation performance in experimental conditions may be slightly better than in design conditions, particularly considering the higher air change rate and lower Richardson number.

The quantitative analysis compared z-direction profiles at five points in the Roman Baths, revealing similar trends in temperature and velocity evolution for both experimental and design conditions, with notable differences in temperature profiles at points 1 to 3. Ratios of temperature or velocity differences at highest and lowest points to building height were calculated for stratification comparison. For experimental conditions, temperature ratios ranged from 0.12 to 0.36, with point 2 having the lowest ratio, indicating lesser stratification. Design conditions showed ratios from 0.10 to 0.32, with similar trends. The experimental conditions demonstrated greater stratification for temperature and velocity parameters compared to design conditions, possibly due to real conditions incorporating factors increasing vertical variation.

Further qualitative analysis of temperature contour maps in XY planes and vector maps in YZ and XZ planes highlighted significant differences in thermal stratification between experimental and design conditions. Experimental conditions exhibited relatively uniform temperature distribution up to a height of 3 m, with increased stratification above this level, particularly near heat sources, resulting in local temperature elevations. Conversely, design conditions showed smoother temperature transitions between heights, with smaller temperature gradients. Velocity maps illustrated airflow patterns and recirculation zones, indicating that while fresh air intake occurred laterally and moved downward to bypass circulation regions' floors, heated air near radiators followed an upward trajectory towards the roof. Despite similar flow patterns, velocity magnitudes were slightly lower in design conditions compared to experimental conditions, suggesting potentially lower ventilation performance in terms of air velocity. Detailed representations of velocity distribution revealed potential recirculation zones, particularly evident in specific planes, which could impact ventilation performance and indoor air quality. Overall, the convergence of results from different evaluation methods indicated performance natural ventilation, with experimental operational conditions showing slight improvement over design operational conditions.

The findings of this study highlight the robustness of the methods used to analyse ventilation performance in large, naturally ventilated spaces, reinforcing the model's reliability across various contexts, even with a limited number of experimental data points. While turbulence models are fundamental to turbulent flow analysis and best practices involve using widely accepted models, a thorough examination of these models is recommended for future research. In the context of this study, where the conditions do not involve highly stratified flows with high velocities, the specific impact of the turbulence models used may be less critical. However, further research could explore the applicability of these findings to different types of large, naturally ventilated spaces and consider a range of turbulence models and discrete formats to enhance the understanding and generalizability of the results.

CRediT authorship contribution statement

Rafaela Mateus: Writing – review & editing, Writing – original draft, Methodology, Investigation, Formal analysis, Conceptualization. **Armando Pinto:** Writing – review & editing, Supervision, Resources, Methodology, Funding acquisition, Conceptualization. **José M.C. Pereira:** Writing – review & editing, Supervision, Software, Resources, Methodology, Funding acquisition, Conceptualization.

Declaration of competing interest

The authors declare that they have no known competing financial interests or personal relationships that could have appeared to influence the work reported in this paper.

Data availability

No data was used for the research described in the article.

Acknowledgements

The authors acknowledge Fundação para a Ciência e a Tecnologia (FCT) for its financial support via the project LAETA Base Funding (DOI: 10.54499/UIDB/50022/2020).

References

[1] D.P. Albuquerque, N. Mateus, M. Avantaggiato, Full-scale measurement and validated simulation of cooling load reduction due to nighttime natural ventilation of a large atrium, Energy Build. (2020) 110233, https://doi.org/10.1016/j.enbuild.2020.110233.
[2] N.R.M. Sakiyama, L. Mazzaferro, J.C. Carlo, T. Bejat, H. Garrecht, Natural ventilation potential from weather analyses and building simulation, Energy Build. 231 (2021) 110596, https://doi.org/10.1016/j.enbuild.2020.110596.
[3] H.L. Gough, J.F. Barlow, Z. Luo, M. King, C.H. Halios, C.S.B. Grimmond, Evaluating single-sided natural ventilation models against full-scale idealised measurements : impact of wind direction and turbulence, Build. Environ. 170 (2020) 106556, https://doi.org/10.1016/j.buildenv.2019.106556.
[4] D. Etheridge, A perspective on fifty years of natural ventilation research, Build. Environ. 91 (2015) 51–60, https://doi.org/10.1016/j.buildenv.2015.02.033.
[5] C.-A. Roulet, Santé et qualité de l'environnement intérieur dans les bâtiments. Presses polytechniques et universitaires Romandes, 2004. http://infoscience.epfl.ch/record/85617.
[6] M. Palme, C. Carrasco, M. Ángel Gálvez, L. Inostroza, Natural ventilation: a mitigation strategy to reduce overheating in buildings under urban heat island effect in south American cities, IOP Conf. Ser. Mater. Sci. Eng. 245 (2017), https://doi.org/10.1088/1757-899X/245/7/072046.
[7] H.Y. Zhong, Y. Sun, J. Shang, F.P. Qian, F.Y. Zhao, H. Kikumoto, C. Jimenez-Bescos, X. Liu, Single-sided natural ventilation in buildings: a critical literature review, Build. Environ. 212 (2022) 108797, https://doi.org/10.1016/j.buildenv.2022.108797.
[8] E. Cuce, F. Sher, H. Sadiq, P.M. Cuce, T. Guclu, A.B. Besir, Sustainable ventilation strategies in buildings : CFD research, Sustain. Energy Technol. Assessments 36 (2019), https://doi.org/10.1016/j.seta.2019.100540.
[9] H. Hu, H. Kikumoto, R. Ooka, C. Lin, B. Zhang, Comprehensive validation of experimental and numerical natural ventilation predictions based on field measurement with experimental house, Build. Environ. 207 (2022) 108433, https://doi.org/10.1016/j.buildenv.2021.108433.
[10] A. Pinto, Ventilação Das Termas Romanas De Chaves - Estudo de estratégias de ventilação e de aquecimento, Lisboa LNEC, relatório n.º 293/2018 - Dep. Edifícios/NAICI, 2018.
[11] Z. Zhai, M. El Mankibi, A. Zoubir, Review of natural ventilation models, Energy Proc. 78 (2015) 2700–2705, https://doi.org/10.1016/j.egypro.2015.11.355.
[12] J.C. Salcido, A.A. Raheem, R.R.A. Issa, From simulation to monitoring: evaluating the potential of mixed-mode ventilation (MMV) systems for integrating natural ventilation in office buildings through a comprehensive literature review, Energy Build. 127 (2016) 1008–1018, https://doi.org/10.1016/j.enbuild.2016.06.054.
[13] A. Aflaki, M. Esfandiari, A review of numerical simulation as a precedence method for prediction and evaluation of building ventilation performance, Sustainability (2021) 1–18, https://doi.org/10.3390/su132212721.
[14] S. Omrani, V. Garcia-Hansen, B. Capra, R. Drogemuller, Natural ventilation in multi-storey buildings: design process and review of evaluation tools, Build. Environ. 116 (2017) 182–194, https://doi.org/10.1016/j.buildenv.2017.02.012.
[15] N. Izadyar, W. Miller, B. Rismanchi, V. Garcia-hansen, Impacts of façade openings ' geometry on natural ventilation and occupants ' perception : a review Air Change

per Hour, Build. Environ. 170 (2020) 106613, https://doi.org/10.1016/j.buildenv.2019.106613.
[16] Y. Li, P. Heiselberg, Analysis methods for natural and hybrid ventilation - a critical literature review and recent developments, Int. J. Vent. 1 (2003) 3–20, https://doi.org/10.1080/14733315.2003.11683640.
[17] G. Remion, B. Moujalled, M. Mankibi, R. Jobert, L. Deleersnyder, Assessing the performance of natural ventilation systems: a review of existing methods, 39th AIVC Conf. Smart Vent, Build (2018).
[18] G. Remion, B. Moujalled, M. El Mankibi, Review of tracer gas-based methods for the characterization of natural ventilation performance: comparative analysis of their accuracy, Build. Environ. 160 (2019) 106180, https://doi.org/10.1016/j.buildenv.2019.106180.
[19] M. Chen Austin, D. Mora, D. Bruneau, A. Sempey, A review of airflow rate estimation techniques for natural ventilation in buildings, Rev. Fac. Ing. Univ. Antioquia. (2021) 1–17, https://doi.org/10.17533/udea.redin.20210849.
[20] G. Carrilho da Graça, P. Linden, Ten questions about natural ventilation of non-domestic buildings, Build. Environ. 107 (2016) 263–273, https://doi.org/10.1016/j.buildenv.2016.08.007.
[21] Z.J. Zhai, Z. Zhang, W. Zhang, Q.Y. Chen, Evaluation of various turbulence models in predicting airflow and turbulence in enclosed environments by CFD: Part 1—summary of prevalent turbulence models, HVAC R Res. 13 (2007) 853–870, https://doi.org/10.1080/10789669.2007.10391459.
[22] H. Zhang, D. Yang, V.W.Y. Tam, Y. Tao, G. Zhang, S. Setunge, L. Shi, A critical review of combined natural ventilation techniques in sustainable buildings, Renew. Sustain. Energy Rev. 141 (2021) 110795, https://doi.org/10.1016/j.rser.2021.110795.
[23] R.C. Adhikari, M. Pahlevani, Characteristics of thermal plume from an array of rectangular straight fins with openings on the base in natural convection, Int. J. Therm. Sci. 182 (2022) 107798, https://doi.org/10.1016/j.ijthermalsci.2022.107798.
[24] World Green Building Council, Every building on the planet must be 'net zero carbon' by 2050 to keep global warming below 2°C – new report, ccessed Febr. 2023, https://worldgbc.org/article/every-building-on-the-planet-must-be-net-zero-carbon-by-2050-to-keep-global-warming-below-2c-new-report, 2023.
[25] European Commission, Climate change and you, Accessed Febr. 2023, https://climate.ec.europa.eu/citizens/climate-change-and-you_en, 2023.
[26] European Commission, Can you afford to heat your home?, Accessed Febr. 2023, https://commission.europa.eu/news/can-you-afford-heat-your-home-2021-01-07_en, 2021.
[27] M. Pinto, F.M. da Silva, J. Viegas, V.P. de Freitas, Sistemas de Ventilação Natural em Edifícios de Habitação . Requisitos para a sua Modelização, Int. Conf. Eng. UBI2011 - Innov. Dev. (2011).
[28] A. Pinto, R. Mateus, J. Silva, M. Lopes, NZEB modular prefabricated building system, Sustain. Autom. Smart Constr. (2021), https://doi.org/10.1007/978-3-030-35533-3_20.
[29] R. Mateus, J.M.C. Pereira, A. Pinto, Natural ventilation of large air masses : experimental and numerical techniques review, Energy Build. (2023) 113120, https://doi.org/10.1016/j.enbuild.2023.113120.
[30] STRONGAXIS Engenharia, Ventilação e Aquecimento das Termas Romanas de Chaves: AVAC, Proj. STRONGAXIS Eng, 2019.
[31] E. 16798-7, Energy performance of buildings - ventilation for buildings - Part 7: calculation methods for the determination of air flow rates in buildings including infiltration. Modules M5-5), CEN, 2018, 2018.
[32] DL 101-D, n Decreto-Lei, º 101-D/2020 de 7 de dezembro, Diário da República - I Série, 2020, pp. 3179–3182.
[33] Manual SCE, Manual Técnico para a Avaliação do Desempenho Energético dos Edifícios, Direção-Geral Energ, Geol. (2021) 252. https://www.sce.pt/wp-content/uploads/2021/07/Manual-SCE.pdf.
[34] M. Samer, C. Loebsin, M. Fiedler, C. Ammon, W. Berg, P. Sanftleben, R. Brunsch, Heat balance and tracer gas technique for airflow rates measurement and gaseous emissions quantification in naturally ventilated livestock buildings, Energy Build. 43 (2011) 3718–3728, https://doi.org/10.1016/j.enbuild.2011.10.008.
[35] J.J. Moghaddam, The effect of turbulence on natural ventilation of a proposed octagonal greenhouse in a transient flow, Int. J. Environ. Sci. Technol. 18 (2021) 2181–2196, https://doi.org/10.1007/s13762-020-02955-y.
[36] E.A. Villagrán, E.J.B. Romero, C.R. Bojacá, Transient CFD Analysis of the Natural Ventilation of Three Types of Greenhouses Used for Agricultural Production in a Tropical Mountain Climate, 2019, https://doi.org/10.1016/j.biosystemseng.2019.10.026, 8.
[37] R. Mateus, A. Pinto, J.M.C. Pereira, CFD methodology for predicting thermal plume from heat source : experimental validation and simplified model, Build. Environ. 257 (2024), https://doi.org/10.1016/j.buildenv.2024.111526.
[38] SIEMENS, Simcenter STAR-CCM+ Documentation - Version 2020.2, SIEMENS, 2020.
[39] N. Padoin, A.T.O.D. Toé, C. Soares, CFD Applied to the Investigation of Flow Resistances in Porous Media, Congr. Interam, Comput. Apl. a la Ind. Procesos, 2014.
[40] C. Specialties, Grille de ventilation. https://www.c-sgroup.fr/products/architectural-louvres/ventilation-louvres/a4085/#hubspot_brochure, December 2023, 2023.
[41] ASHRAE, Heating, ventilating, and air-conditioning APPLICATIONS, ASHRAE Handb (2019) 1357.
[42] O.O. Smedegård, B. Aas, J. Stene, L. Georges, Measurement and analysis of evaporation in indoor swimming pools: comparison with the ASHRAE' s activity factor, E3S Web Conf. 362 (2022) 1–7, https://doi.org/10.1051/e3sconf/202236214004.
[43] Thermoworks, emissivity table. https://www.thermoworks.com/emissivity-table/, December 2022, 2023.
[44] Y. Cengel, M. Boles, M. Kanoglu, Thermodynamics - an Engineering Approach, 9, McGraw-Hill Education, New York, 2019.
[45] MatWeb, aluminum 3003-H12. https://www.matweb.com/search/DataSheet.aspx?MatGUID=5b30b87291e84c5e843a9b0025b7dfc6, December 2022, 2022.
[46] ASHRAE, ASHRAE Fundamentals Handbook- Chapter 6: Psychrometrics, ASHRAE Handb, 2001.
[47] F. Rojano, P.E. Bournet, M. Hassouna, P. Robin, M. Kacira, C.Y. Choi, Modelling the impact of air discharges caused by natural ventilation in a poultry house, Biosyst. Eng. 180 (2019) 168–181, https://doi.org/10.1016/j.biosystemseng.2019.02.001.
[48] P.P. Roy, S. Chowdhury, M.H. Raj, M.Q. Islam, S. Saha, Forced, natural and mixed convection of Non-Newtonian fluid flows in a square chamber with moving lid and discrete bottom heating, Results Eng 17 (2023) 100939, https://doi.org/10.1016/j.rineng.2023.100939.
[49] Y. Wang, T. Zhao, Z. Cao, C. Zhai, S. Wu, C. Zhang, Q. Zhang, W. Lv, The influence of indoor thermal conditions on ventilation flow and pollutant dispersion in downstream industrial workshop, Build. Environ. 187 (2021) 107400, https://doi.org/10.1016/j.buildenv.2020.107400.
[50] L.G. Carreto-Hernandez, S.L. Moya, W.G. Báez-García, L.C. Sandoval Herazo, A. Francisco-Hernandez, J.C. Hernández-Jerónimo, E. Téllez-Velázquez, Numerical-experimental investigation of a wind tower-room sustainable system: a parametric analysis of the mixed convection with humidification, J. Build. Eng. 91 (2024), https://doi.org/10.1016/j.jobe.2024.109624.
[51] IPMA, Inst. Port. do Mar e da Atmos, Ficha Climatológica, https://www.ipma.pt/pt/oclima/normais.clima, 2024.